ATR-FTIR MEASUREMENTS OF CATIONIC SURFACTANT EXCHANGE RATES AT THE SOLID-LIQUID INTERFACE

Spencer C. Clark

Thesis presented to the Faculty of
Virginia Polytechnic Institute and State University
in partial fulfillment of the requirements for the degree of

Master of Science
in Chemistry

APPROVED:

William A. Ducker, Chair

Mark R. Anderson

Alan R. Esker

21 July 2003
Blacksburg, Virginia

Keywords: Surfactant, Adsorption, Kinetics, ATR-FTIR

ATR-FTIR MEASUREMENTS OF CATIONIC SURFACTANT EXCHANGE RATES AT THE SOLID-LIQUID INTERFACE

Spencer C. Clark

ABSTRACT

In many experiments, surfactant adsorption and desorption at solid-liquid interfaces is found to be quite slow, considering that surfactants are small molecules. Attenuated total reflectance Fourier transform infrared spectroscopy was used to study the adsorption, desorption, and exchange of tetradecyltrimethylammonium bromide (C_{14}TABr) at the silicon oxide surface. The exchange of surfactant was monitored using protonated and perdeuterated C_{14}TABr. The data show that exchange of C_{14}TABr between the surface and the bulk solution is very fast, complete exchange occurs in less than 10 seconds. A simple exchange model suggests that the disassociation rate constant of a single monomer is no less than 1 s^{-1}, which is ~ 10^4 times slower than monomer exchange in bulk solutions. The actual exchange rate may be greater than observed in the present work due to transport phenomena. The rates of exchange are similar at concentrations above and below the critical micellar concentration. Adsorption is similarly rapid, but under some circumstances there is a small residue of surfactant that is slow to desorb. Desorption experiments utilizing KBr solutions of high and low ionic strength show that two thirds of each adsorbed micelle is held by hydrophobic association, and the other third is electrostatically bound. Adsorption, desorption, and exchange experiments at temperatures of 11°C above and 8°C below the Krafft temperature (14.4°C) show similar kinetics.

Acknowledgments

My physical chemistry professor at Utah State University often remarked that knowledge is either discovered or invented (depending on ones own personal perspective). I never figured out what he thought on the matter, but I found it an interesting concept that I had never considered. I believe that we are only discovering what the Creator of the universe already knows, and as it says in the scriptures, in reference to the order of the universe, "Behold, all these are kingdoms, and any man who hath seen any or the least of these hath seen God moving in his majesty and power." One of the fascinating aspects of chemistry is to observe God moving in his majesty. The complexity and detail of His creations are stunning, even down to the atomic level. Surely He has created all that we see, and understands all we seek to comprehend. I consider it a privilege to work at elucidating the details of what God already knows, whether it be science or a better understanding of who God is, and what are the most important things we can take with us from our mortal existence. In some sense I graze on both sides of the fence. I have the privilege of working with some wonderful people in the secular community; all are examples of academic, intellectual, and moral stature. I also love the satisfaction and understanding that comes from the study of God in the scriptures. Science is valuable and fascinating to me, but the scriptures teach us what is most important in life. I believe it is people that matter most. Below is a list of educators (in chronological order) that saw more in me than I believed I was capable of accomplishing, who took an interest in me as an individual, and as a student. Those listed may never read this, or receive personal thanks for their efforts, but they deserve recognition none the less. I owe them much.

Dr. William A. Ducker: An Uncommon Man.
Dr. Darla K. Graff: Los Alamos National Labs
Dr. Ed A. McCoullough Jr.: Physical Chemistry, Utah State University
Dr. William Moore: Physical Chemistry Laboratory, Utah State University
Dr. Chuck Carpenter: Food Science and Technology, Utah State University
Dr. Erika Daines: Assistant Professor of Foreign Language, Weber State University
Dr. Richard Vandenburg: Autobody, Weber State University
Mrs. Graham: Trigonometry, Kaysville Jr. High
Mrs. Crawforth: Farmington Elementary School
Mrs. Lacy: Hilltop School, Farmington, Utah
Mrs. Rigtrup: Hilltop School, Farmington, Utah

Table of Contents

List of Figures

List of Tables

Chapter 1 Introduction

Association of molecules in solution to form "colloidal electrolytes" was studied by McBain and Salmon between 1910 and 1920. McBain's research focused on conductivity and anomalous colligative behavior of soap solutions.[1] The phenomena observed by McBain were due to the formation of micelles as the soap solutions reached the critical micellar concentration. In 1936 Hartley proposed the spherical model of a surfactant micelle.[2] Gruen published a sodium dodecylsulfate representation based on a mathematical model developed in 1985. The relationship between micellar geometry and the physical dimension of the surfactant molecule was described by Israelachvili in the late 1970's. The dynamic nature of micelles was demonstrated in 1965 using pressure jump techniques by Mijnlieff.[3] Other experiments such as temperature jump, ultrasound absorption and stopped flow techniques led to the discovery of two distinct micellar kinetic processes, the rapid exchange of monomers between the bulk solution and the micelle, and the relatively slow process of micelle formation and dissolution.

Surfactant behavior at interfaces is of increasing interest, due to the complexity of industrial processes and the desire to control physical and chemical processes at the molecular level.
The characterization of colloidal electrolyte or surfactant behavior in bulk seems to precede characterization at interfaces (solid-liquid, liquid-liquid, or gas-liquid). Surfactant behavior at interfaces often parallels that of the bulk behavior, but the charge at a solid surface (metal oxides, silica, alumina, mica, zeolites, etc.) will perturb the structure and kinetics to some degree.[4] Some aspects of interfacial aggregation have not been entirely characterized. One example is the structure of cationic surfactants at the silica-solution interface.[4-7] There is some uncertainty concerning the molecular structure of surfactant aggregates at the silica-solution interface. Even less is known about the kinetics of surfactants adsorbed at the silica-solution interface. The present work explores the dynamic aspects of trimethylammonium bromide surfactant adsorption, exchange, and desorption at the solid-liquid interface.

A survey of analytical methods available led to the conclusion that Fourier Transform Infrared Total Attenuated Reflection (ATR-FTIR) was a good method for the study of interfacial phenomena. In addition, recent research on the nature of evanescence provides us with an improved understanding of evanescent behavior at multilayer interfaces,[8,9] and allows us to quantitate the amount of surfactant at the silica-solution interface more accurately.

Chapter 2 LITERATURE REVIEW

2.1 BULK SURFACTANT KINETICS

Surfactants influence a number of equilibrium physical properties, such as surface tension, osmotic pressure, solubilization, and turbidity.[10] Surfactant *kinetics* determine the rate at which a surfactant solution can respond to a perturbation to the equilibrium state, such as stabilization of bubble formation, rate of oil solubilization, foaming, or fabric wetting time.[11] This thesis is concerned with the kinetics of adsorption, exchange, and desorption of a cationic surfactant at the silica-solution interface. This literature review will address kinetics of bulk micelles, and micelles adsorbed at the solid-liquid interface. This review is to provide an understanding of surfactant kinetics and an appreciation for the differences between the two systems.

Gruen's theoretical model of a sodium dodecylsulfate micelle is shown in Figure 1.[12 13] The head groups lie at the micelle-water interface and the tails aggregate to form a fluid-like hydrophobic core.

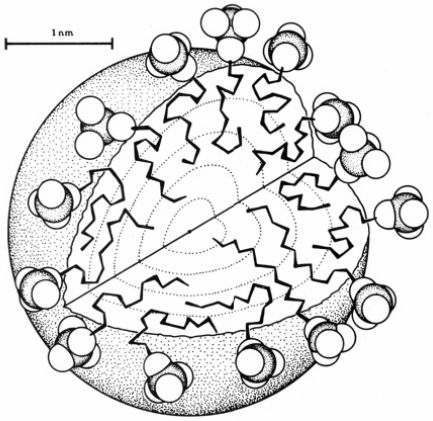

Figure 1. Drawing of a spherical dodecyl sulfate micelle illustrating the location of head groups, and packing of aliphatic tails in the micelle interior. Reprinted with permission from *J. Phys. Chem. B* **1985,** *89*, 146-153. Copyright 1985 American Chemical Society.

Figure 1 is a static representation of a sodium dodecyl sulfate micelle. Experiments show that monomers typically spend several microseconds within a micelle before diffusing back into solution. The time a monomer spends in the micelle is the residence time, and is related to the fast relaxation time, τ_1.[14,15] Micelles are continually forming and dissipating. The micelle lifetime is the average time a micelle is in existence, and is related to the slow relaxation time, τ_2. Both the fast and slow relaxation times influence the response of a surfactant solution to a perturbation. The system's equilibrium state may be perturbed by the rapid creation of new interfacial area, temperature change,

pressure change, or a change in concentration. If one of the state variables of the micellar solution is changed, the distribution of surfactant between micelles and monomers in solution will seek the new equilibrium condition in a two-step process. First, micelles will shed or incorporate monomers in an attempt to reach a new equilibrium aggregation number, *s*. This occurs at a relatively high rate shifting the aggregation number of all micelles away from the optimal value of ~70 for C_{14}TABr in bulk solution.[16,17]

$$A_1 + A_{s-1} \underset{k_s^-}{\overset{k_s^+}{\rightleftharpoons}} A_s \qquad (1)$$

A_1 is the surfactant monomer, A_{s-1} the surfactant micelle with aggregation number *s-1*, and A_s the surfactant micelle with aggregation number *s*. The variables k_s^+ and k_s^- are the monomer association and disassociation constants respectively. Only a finite number of monomers will diffuse from the micelle at the τ_1 rate, because the aggregation number will be maintained to some degree.[11]

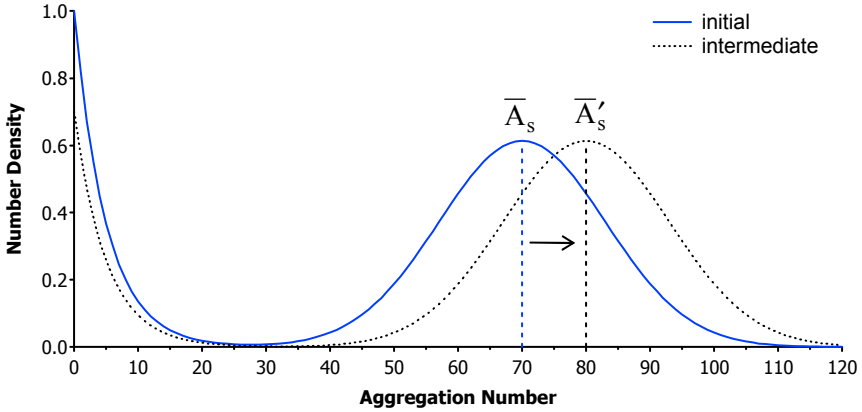

Figure 2. An illustration of the fast relaxation process. Monomers migrate into existing micelles during the fast relaxation process. A perturbation of the equilibrium state causes the aggregation number $\overline{A}_s$ to jump to a higher value $\overline{A}'_s$, reducing the quantity of monomers in solution.

The second process (τ_2) involves a change in the *number* of existing micelles: new micelles are created or destroyed. The process of redistribution of monomers from the dispersing micelle to the other micelles proceeds monomer by monomer, until equilibrium is established.[10] Dimers and trimers invariably contribute to the flux, but the flux is dominated by monomers.[15] At concentrations greater than ten times the critical micellar concentration (cmc), fusion and fission of micelles also contributes to changes in aggregation numbers of ionic micelles.[18,19]

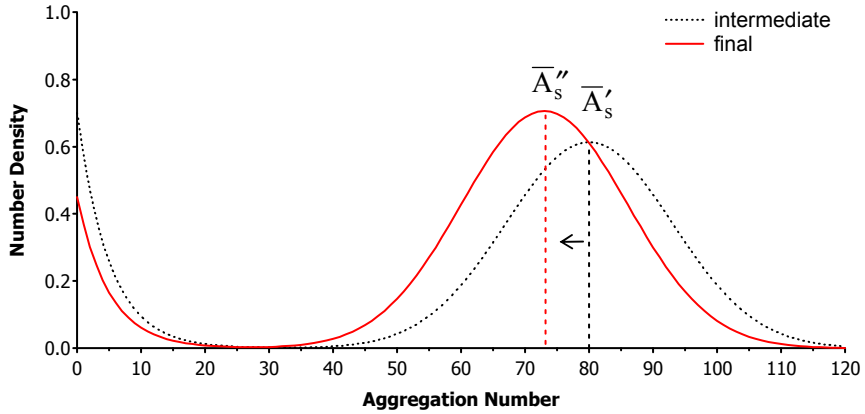

Figure 3. Illustration of the slow relaxation process. Micelles with aggregation number $\overline{A}_s'$ will shed monomers in an attempt to reach a new ideal aggregation number, $\overline{A}_s''$. New micelles with aggregation number $\overline{A}_s''$ form from monomer surplus.

Completion of the second process marks the establishment of equilibrium. The existence of energetically unfavorable aggregation states hinders the breakup of micelles so $\tau_2 > \tau_1$ and is on the order of milliseconds.

2.1.1 Fast Relaxation Time

Fast relaxation, τ_1, is a function of the disassociation constant k^-, the aggregation number n, with standard deviation s, and c_0 which is the average relative deviation of the micelles from equilibrium which is usually less than 1%.[15]

$$\frac{1}{\tau_1} = \frac{k^-}{\sigma^2} + \frac{k^-}{n} a(1 + c_0) \tag{2}$$

a is a function of the equilibrium monomer concentration $\overline{A}_1$, and the total surfactant concentration A_{tot}.

$$a = \frac{(A_{tot} - \overline{A}_1)}{\overline{A}_1} \tag{3}$$

c_0 is a function of the mean aggregation number, and the relative deviation from equilibrium.

$$c_0 = \frac{\sum \xi_s \overline{A}_s}{\sum \overline{A}_s} \tag{4}$$

The relative deviation from equilibrium is calculated from the following expression.

$$\xi_s = \frac{A_s - \overline{A}_s}{\overline{A}_s} \tag{5}$$

Disassociation constants are determined by ultrasonic absorption, stopped flow, and shock tube experiments. Association constants for bulk micelles formed from surfactants with alkyl chains less than or equal to 14 tend to be on the order of 5×10^9 M^{-1} s^{-1}. This value is close to the calculated rate for diffusion.[20] Ultrasonic methods employed by Frindi [21-23] show that the k^+ rate constant is very near those one would expect for diffusion.

Gharibi, et al. determined disassociation constants for C_{10}TABr, C_{12}TABr, and C_{14}TABr as 3.0×10^8 sec^{-1}, 9.5×10^8 sec^{-1}, and 6.6×10^5 sec^{-1}, respectively. The residence time of a surfactant monomer within the micelle is equal to n/k^-. Residence times for the cationic surfactants C_{10}TABr, C_{12}TABr, and C_{14}TABr are 130 ns, 5.2 µs, and 100 µs, respectively.[17] The data show a correlation between hydrocarbon tail length and increasing residence times that hold for all types of surfactant, due to the activation energy for pulling the alkyl chain from the hydrocarbon environment of the micellar core to water.[14]

2.1.2 Slow Relaxation Time

The slow relaxation τ_2 is a function of the same variables as fast relaxation.

$$\frac{1}{\tau_2} \approx \frac{n^2}{\overline{A}_1 R}\left(1 + \frac{\sigma^2}{n} a\right)^{-1} \tag{6}$$

The variable is R, the micellar resistance to passing through unfavorable aggregation numbers as the micelle dissipates (saddle region in Figures 2 and 3). The dissociation constant at each aggregation number is k_s^-, and the concentration of micelles with aggregation number s is $\overline{A}_s$.

$$R = \sum_{s = s_1 + 1}^{s_2} \frac{1}{k_s^- \overline{A}_s} \tag{7}$$

Average micellar lifetimes can be determined using the following relationship.[14]

$$T_{micelle} = \tau_2 n a\left(1 + \frac{\sigma^2}{n} a\right)^{-1} \tag{8}$$

Micellar solutions with long micelle lifetimes (large τ_2 values) equilibrate slowly following a perturbation to the (cmc) or equilibrium distribution of monomers and micelles.[11]

Long micelle lifetimes influence the rate of oil solubilization, emulsion droplet size, bubble size, and interfacial wetting time. Oil solubilization rate increases with micelle lifetime.[24] Emulsion droplet size and gas bubble size is greater when micellar lifetime is longer. The latter two perturbations require a flux of monomers to stabilize newly created interfacial area. The more stable micelles do not readily dissipate, shedding only a finite number of monomers, leaving a limited quantity of micelles available to migrate to the interfacial region.[25] Less surfactant is available to stabilize the interfacial regions, resulting in larger bubble and emulsion droplet size (to minimize the surface area in contact with the surfactant solution). A maximum in the interfacial wetting time corresponds with the maximum in the micellar lifetime.[11]

2.2 WAVENUMBER STUDIES

The position of the asymmetric and symmetric stretching bands gives some indication of the surfactant conformation and the surrounding environment. As a surfactant molecule goes from a monomer in solution to either a bulk micelle or to a micelle at the solid-liquid interface, the peak position of the CH_2 asymmetric stretch will move to lower wavenumber. This shift to lower wavenumber has generally been attributed to a decrease in the number gauche conformations in the tail, as the surfactant becomes more "crystalline."[26,27] There is evidence to show that the shift to lower wavenumber is not strictly related to the degree of trans-conformations in the aliphatic tail.[28] Although wavenumber is not a rigorous indicator of surfactant state, it still can serve as a qualitative guide.

2.3 SURFACTANTS AT THE SOLID-LIQUID INTERFACE

2.3.1 Critical Surface Aggregation Concentration

The critical surface aggregation concentration (csac) is the surface analogue of the cmc. In most situations, surfactants will begin to aggregate at the solid-liquid interface at concentrations between 60% and 80% of the cmc.[29,30] Above the cmc the surface aggregates do not change much with concentration because the chemical potential is a weak function of concentration.

2.3.2 Surface Aggregate Characterization

Atomic force microscopy (AFM) has been used to characterize surface aggregation. The primary advantage of AFM is the ability to acquire three-dimensional structural information. Aggregation numbers, micellar size, shape and surface excess values can be estimated from AFM images.[31]

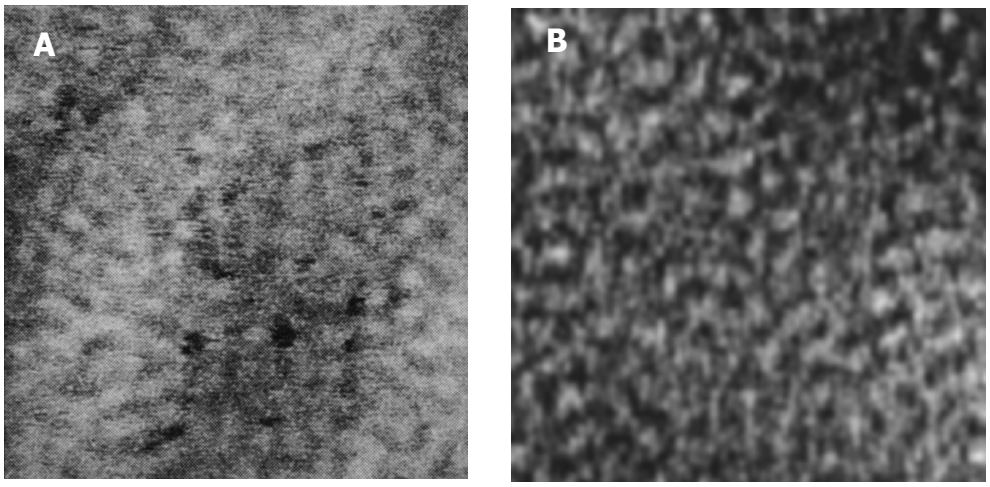

Figure 4. 100 × 100 nm Images of trimethylammonium bromides on silica. **A**. C_{14}TABr. The surfactant concentration was 7.0 mM, (2 × cmc).[32] The solution pH was 2.9. Reprinted with permission from *Science* **1995** December 1, *270*, 1480-1482. Copyright 1995 American Association for the Advancement of Science. **B**. C_{16}TABr aggregates at 2.0 mM (2 × cmc). Reprinted with permission from *J. Phys. Chem. B* **1999**, *103*, 8558-8567. Copyright 1999 American Chemical Society.

Using AFM, Manne showed that C_{14}TABr adsorbs as spheroids or spherical micelles.[33] Liu and Ducker show that surface aggregates for C_{14}TABr and C_{16}TABr are spherical in solution and relatively unperturbed by adsorption to silica.[4]

Neutron reflectivity studies provide information that is complementary to AFM images. Both Rennie and McDermott studied aggregation of trimethylalkylammonium bromide to silica.[34,35]

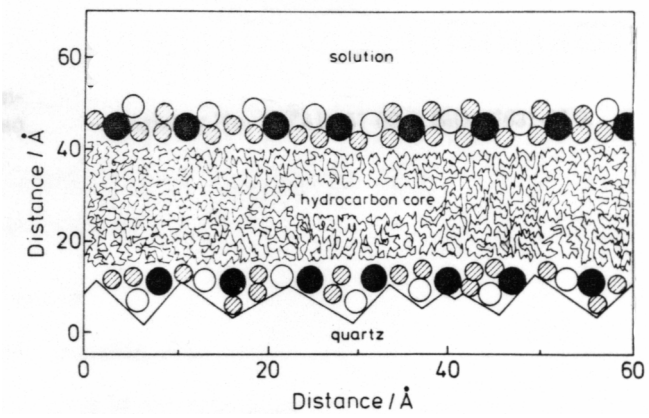

Figure 5. Structure of adsorbed C_{16}TABr at the silica water interface from neutron reflectivity experiments. Reprinted with permission from *Langmuir* **1990,** *6*, 1031-1034. Copyright 1990 American Chemical Society.

Their data show the formation of surface aggregates with head groups concentrated in two planes, (1) at the silica surface and (2) facing the aqueous solution. The C_{16} aliphatic tails were sandwiched between the two headgroup layers. Bromide counter ions were found concentrated near the ammonium headgroups. Work done by McDermott et al. on the same system utilized deuterium labeling to improve resolution of the head and tail regions.[35]

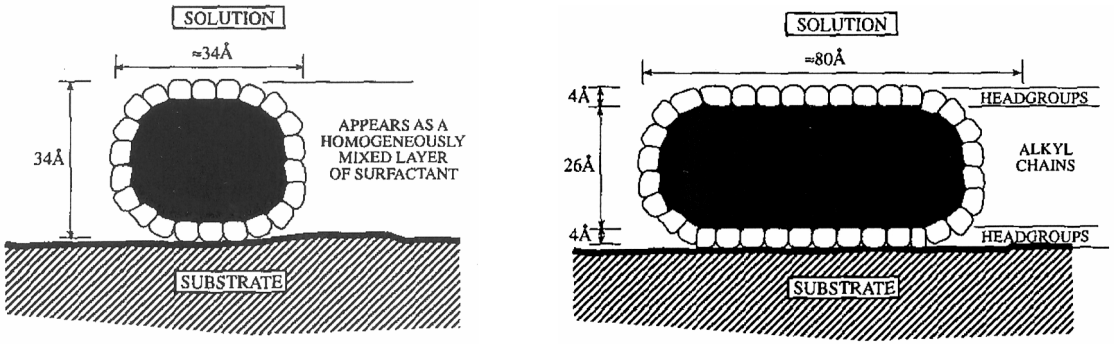

Figure 6. Cross sectional views of C_{16}TABr adsorbed at the silica-solution interface obtained by neutron scattering A. Surfactant concentration of 0.3 mM (0.4 × cmc). B. Surfactant concentration of 0.9 mM (0.95 × cmc). Resolution of head and tail regions was accomplished by isotopically labeling portions of the surfactant molecule. Reprinted with permission from *Jnl of Colloid and Interface Sci* **1994,** *162*, 304-310. Copyright 1994, with permission from Elsevier.

The time scale for acquisition of an AFM image or a neutron scattering profile is on the order of minutes. The AFM experiments imply that the surface aggregates have long τ_2 times.

2.3.3 Bulk and Interfacial Aggregation Numbers

Gharibi et al. used surfactant selective electrodes to show that the bulk aggregation number of C_{14}TABr was 66 ± 4.[17] Hansson used fluorescence quenching to obtain an aggregation number of 74.[16] Other fluorescence quenching work puts the aggregation number between 58 and 93 depending on the analytical method used.[36]

Micelles adsorbed at the solid-solution interface have aggregation numbers between one and two times their bulk counterparts. An analysis of Manne's AFM experiments[32] published by Ström[31] show an aggregation number of roughly 85 ± 18. Ström's research on surface aggregation numbers for C_{14}TABr surfactant using fluorescence quenching estimated an aggregation number of between 53 and 143, at concentrations of 1.0 mM (0.3 × cmc) and 3.1 mM (0.9 × cmc) respectively. Table 1 contains surface aggregation numbers for other trimethylammonium bromide surfactants as a function of cmc.

Table 1. Aggregation Numbers of Trimethylammonium Bromide Surfactants. [31] Bulk aggregation numbers are also listed for the same probe-quencer combination used in the silica interface study.

Surfactant	Conc. /mM	Salt Conc. /mM	N (surface)	N (bulk)
C_{12}TABr	5.1	0	40	
	10.1	0	59	
	14.1	0	82	60
	5.1	50.0	54	
	5.1	100.0	64	
C_{14}TABr	1.0	0	35	
	2.0	0	72	
	3.0	0	115	
	3.1	0	143	80
	1.0	5	93	
C_{16}TABr	0.8	0	93	75-120

In a study of $C_{16}TA^+$ adsorption and desorption from a silica interface, Velegol et al. indicate that aggregation numbers in bulk solution are less than surface aggregation numbers.[37] Velegol also considered the possibility that micelles can adsorb directly to the solid-liquid interface. At concentrations above the cmc, direct adsorption of micelles to the surface would perturb its aggregation number (and possibly micellar shape).

2.3.4 Effect of Surface Charge on Adsorbed Micelles

In addition to the study of $C_{16}TA^+$ adsorption to silica Velegol et al. compared AFM images of $C_{16}TA^+$ on mica to images of CTA^+ on silica, to deduce the effect of surface charge on the aggregate structure.[37] Aggregates on silica (lower charge density than mica) were spaced further apart than their counterparts on mica. The silica adsorbates had a greater axial curvature, and more pronounced structural transitions were observed as the counterion was switched from bromide to chloride.

2.3.5 Surface Aggregate Kinetics

My thesis focuses on the kinetics of ionic surfactant processes at the solid-solution interface. There are three basic processes studied in the present work. First, exchange of surfactant with adsorbed solvent or ions (adsorption experiments). Second, exchange of surfactant for another surfactant (exchange experiments). Finally, exchange of solvent or small ions (desorption experiments).

2.3.5.1 The Adsorption Process

Figure 7 illustrates the initial adsorption process. At time zero, surfactant migrates from the bulk to the solid interface. As the surface excess increases, the reverse rate will begin to rise from its initial zero value. Adsorption experiments allow us to determine the association rate constant, k^+. One must keep in mind that all sites at the solid surface are undergoing some type of exchange, for every surfactant molecule that adsorbs a solvent must desorb. In addition, ions may desorb when a

charged surfactant adsorbs. The ion charge, size, or other chemical properties may exert some control of the kinetic process.

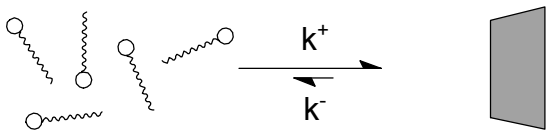

Figure 7. The adsorption process at time = zero. The forward rate is observed during adsorption, and is transport limited for small molecules.

The observed initial rate of surfactant adsorption at the solid-liquid interface is transport limited. Adsorption of sodium laurate to alumina was investigated by Couzis using ATR-FTIR. An analysis of the kinetics by plotting absorbance with respect to square root of elapsed time is linear, which is consistent with a diffusion limited system.[38] Tiberg studied adsorption of nonionic surfactants to silica using ellipsometry. Experimental data and an analysis of diffusive transport show that adsorption of monomers (and micelles when the concentration is above the cmc) is controlled by diffusion through a stagnant layer at the surface.[30] Eskilsson investigated C_{16}TABr adsorption of using ellipsometry.[39] Their results show that the adsorption rate is concentration dependent below the cmc, ranging in times from several minutes to two hours. The kinetics become diffusion limited at the lowest concentrations investigated. At concentrations equal to and greater than the cmc, the rate corresponds to 10^{-11} (mol/cm^2)/sec.

Ionic surfactants kinetics are influenced by mass transfer in solution. Migration results from the native charge on the solid substrate, attracting adsorbates of opposite charge. At some point the surface charge is neutralized by adsorbing surfactant, and any further adsorption by surfactant will cause charge reversal. Once charge reversal occurs, additional surfactant must adsorb against electrostatic repulsion, and the rate decreases.[40] Electrostatic repulsion will reduce the rate of diffusion by a factor of ten for ionic systems, compared to non-ionic systems.[41] Pagac showed that increasing the ionic strength above that of the surfactant and counterion increases the rate of adsorption.[40] Diffusion occurs as a result of a chemical potential gradient in the solution. Forced convection (exchange of solution by pumping) also influences the rate of transport to the silica-solution interface in the present study.

There is a whole body of research pertaining to surfactant adsorption kinetics that have employed solution depletion methods to determine kinetic rates.[42-44] These experiments are initiated by mixing a slurry of surfactant and silica. Data collection is by aliquot withdrawal at fixed-time intervals, followed by centrifuging and quantitation by UV-Vis or HPLC. Time resolution for these experiments ranged from two minutes to about an hour. Kinetic rates obtained by Biswas were on

the order of 0.2 to 0.8 min^{-1} using a similar technique for C_{12}, C_{14}, and C_{16}TABr. Using the same methods of Li and Biswas, Ghosh showed that the kinetics were in fact diffusion limited. Results were given in terms of diffusion constants.[45] The much longer time constants measured for particulate systems suggest that these experiments actually measure diffusion of surfactants through the particulate sediment. Therefore, in most cases these experiments provide no information about adsorption kinetics.

2.3.5.2 The Exchange Process

The equilibrium exchange process is illustrated by Figure 8. This exchange does not change the quantity of surfactant in the bulk or at the surface, but there is exchange of surfactant between the two regions.[46,47] The rate of this process has not been previously measured.

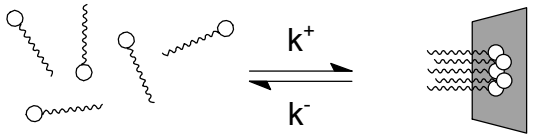

Figure 8. Dynamic exchange of surfactant between bulk solution and the surface.

2.3.5.3 The Desorption Process

Figure 9 shows the desorption kinetics. By rapidly flushing away the bulk surfactant solution and replacing it with water, the adsorption drops to zero, and one can observe the surfactant flux away from the interface. Charged sites vacated by desorbing surfactant must be occupied by other ions from the solution.

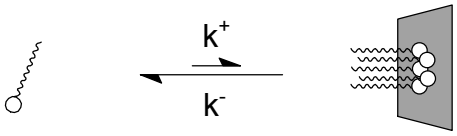

Figure 9. Desorption process. Forward rate is reduced to near zero as the bulk solution is replaced by pure solvent.

Tiberg studied desorption using a series of hexaethylene glycol monoalkyl ethers with C_{12}, C_{14}, and C_{16} tail lengths. Desorption was independent of surfactant concentration, but desorption times increased with increasing tail length.[30] Desorption of C_{16}TABr from silica using ellipsometry was shown to be independent of concentration and complete within a few *minutes*. The initial rate of adsorption is roughly equal to the experimentally determined desorption rate of 1×10^{-11} $(mol/cm^2)/sec$.[39] Atkin et al. show that desorption of C_{16}TABr with salt and water leads to complete

removal of the adsorbate within hundreds of seconds. Adsorption, in contrast, required only about 20 seconds.[48] Velegol et al. observed desorption using reflectometry with a resolution of several seconds and claim that desorption was complete within seconds.[37] Neivandt's ATR-FTIR adsorption and desorption studies of C_{16}TABr on silica show that the surfactant will not desorb entirely, it drops to about 15% of the maximum value, even after rinsing for 20 hours.[49,50]

Chapter 3 ATR-FTIR THEORY

3.1 ATR-FTIR AS AN IN-SITU SURFACE SELECTIVE ANALYTICAL TOOL

ATR-FTIR can be used to determine refractive index, surface excess, spectral identity, and molecular orientation *in situ* at the solid-liquid interface. Depending on the capabilities of the instrument, kinetic resolution is on the order of seconds to hundredths of a second. One challenge of quantitation using ATR-FTIR is calculation of the electric field intensities in the x, y, and z directions at the evanescent interface.

3.2 SELECTION OF THE OPTIMAL MATHEMATICAL MODEL

Much of the ATR experimental work relies on the approximate two and three phase equations for determining the mean square electric fields derived by Harrick.[51,52] Others have opted for the more rigorous derivations by Wilford Hansen.[53-55] Hansen's derivations take into account the complex refractive indices of both the intermediate and final layers and the distance of the absorber from the internal reflection interface. Until recently, there has been no experimental evidence to suggest that one derivation or model was superior to the other. Neivandt assessed the validity of Harrick's two and three phase models for determining the dichroic ratio of C_{16}TABr adsorbed at the silica solution interface. They concluded that the Harrick three phase model did not give feasible dichroic ratios.[49] Axelsen and Picard both conducted a thorough evaluation of both Harrick and Hansen's two and three phase equations. Using proteins adsorbed to a trichlorosilane monolayer, Axelsen found neither Harrick nor Hansen's three phase models were accurate representations of evanescent wave electric field strength at a stratified medium when the intermediate layers were only tens of nanometers thick.[8] The most accurate derivations for calculation of mean square electric fields are the two phase models.[9,56]

In the present work, Hansen's two phase equations were used for two reasons. First, Hansen's derivation uses complex refractive indices, which allow one to include the absorption coefficient of the semi-infinite final phase and intermediate phases of the system. Harrick assumes that the intermediate and semi-infinite final phases are non-absorbers. Water and deuterium oxide are both infrared active, so Hansen's model is more realistic. Second, the Hansen equations allow for decay of the mean square electric field strengths as a function of distance from the evanescent interface.

3.3 QUANTITATIVE DETERMINATION OF GIBBS SURFACE EXCESS VIA ATR

The Gibbs surface excess, Γ, of the surfactant at the interface between the silicon reflection element and the surfactant in D_2O solution was determined using the following expressions.[55,57-61]

$$-\log(R) = N\varepsilon C_{bulk} b_{eff} + N\varepsilon \frac{b_{eff}}{d} \Gamma \tag{9a}$$

$$-\log(R) = N\varepsilon \frac{b_{eff}}{d} \Gamma^* \tag{9b}$$

-log(R) is the absorbance of the CH or CD stretching band, integrated over the entire band. N is the number of internal reflections, ε is the transmission molar absorption coefficient of the surfactant CH and CD stretching bands, and C_{bulk} is the concentration of surfactant in bulk solution. b_{eff} is the effective penetration depth, and d is the decay length of the evanescent wave in the aqueous medium. The first term on the right hand side of Equation 9a arises from bulk contributions and in equilibrium measurements can be calculated from bulk measurements. In kinetics experiments, the bulk concentration is not known, so the entire absorption is attributed to the surface. This error is acknowledged by the use of Γ* for kinetic measurements.

These equations assume isotropic orientation for bulk and surface adsorbed surfactant. Anisotropic orientation of surface aggregates may introduce some quantitative errors. Mathematical models[12] of various aggregate geometries (spheres, cylinders, hemi-sphere atop a monolayer, and hemi-cylinder atop a monolayer) all have CH transition dipole moment distributions that are nearly isotropic.

The shape and position of the absorption peak depend on the environment of the surfactant (see Figure 11) so the use of absorption at a single frequency in equation 9a could introduce artifacts arising from changes in surfactant environment. Therefore, the integrated reflectance of the entire peak was used.

3.3.1 Mean Square Electric Field Strengths of the Evanescent Wave

The optical properties of the interface are modeled as a three layer system, where the subscripts 1, 2, and 3 refer respectively to the silicon reflection element, the immediately adsorbed surfactant layer, and the bulk solution.

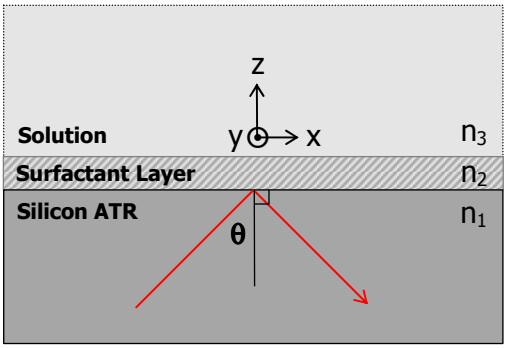

Figure 10. Sketch of the silicon, surfactant, solution interface. Infrared radiation has incident angle θ, measured with respect to the n_1, n_2 interface normal. The electric vector of p-polarized infrared radiation lies in the plane of the page, the evanescent wave (in phase n_2, and n_3) has electric field components in the z and x directions (with respect to the coordinate reference frame). The electric vector of the s-polarized radiation is perpendicular to the plane of the page, the evanescent wave electric field (in phase n_2, and n_3) lies in the y-direction.

The penetration depth, d, is determined from the expression:

$$d = \frac{\lambda}{4\pi \,\mathrm{Im}(\xi_3)} \tag{10}$$

where λ is the infrared radiation wavelength, and ξ_j is defined in equation 11a for phase 2 and 3. Note that the penetration depth is calculated using ξ_3, from equation 11a. The complex refractive index is defined as $\hat{n}_j = n_j + ik_j$, where n_j is the real refractive index and k_j the absorption coefficient.

$$\xi_{j=2,3} = \left[\hat{n}_j^{\,2} - n_1^{\,2}\sin^2(\theta)\right]^{\frac{1}{2}} \tag{11a}$$

$$\xi_1 = \hat{n}_1 \cdot \cos\theta \tag{11b}$$

The effective path length, b_{eff}, is a function of the bulk medium refractive index, n_3, and the incident angle θ. The effective path length is polarization dependent, the s-polarized, and p-polarized values are calculated from equations 12a and 12b, respectively.[55,58] The time averaged mean square electric

amplitudes in phase n_3 at the total internal reflection interface in the x, y, and z directions $\left\langle E_x{}^2 \right\rangle$ $\left\langle E_y{}^2 \right\rangle$ and $\left\langle E_z{}^2 \right\rangle$ are required to quantify surfactant adsorption.

$$b_{\text{eff, s}} = \frac{d\left\langle E_y{}^2 \right\rangle_{z=0} n_3}{n_1 \cos\theta} \tag{12a}$$

$$b_{\text{eff, p}} = \frac{d\left\langle E_x{}^2 \right\rangle_{z=0} n_3}{n_1 \cos\theta} + \frac{d\left\langle E_z{}^2 \right\rangle_{z=0} n_3}{n_1 \cos\theta} \tag{12b}$$

The subscripts *s* and *p* refer, respectively, to the electric field polarized perpendicular and parallel to the plane of incidence. The effective path length [62] $b_{\text{eff, unp}}$, is dependent on the spectrometer polarization ratio PR, which is unique to the instrument and is experimentally determined.[63]

$$b_{eff,\,unp} = \frac{PR \cdot b_{eff,\,s}}{PR+1} + \frac{b_{eff,\,p}}{PR+1} \tag{13}$$

Hansen has published the most comprehensive equations for determining mean square electric amplitudes for an evanescent wave as a function of distance from the interface and the complex refractive index of the intermediate and final phases. [8,9,53-55]

$$\left\langle E_x{}^2 \right\rangle = \left| \frac{t_p}{\hat{n}_3} \xi_3 \right|^2 \exp\left(-\frac{(z-h)}{d} \right) \tag{14}$$

$$\left\langle E_y{}^2 \right\rangle = \left| t_s \right|^2 \exp\left(-\frac{(z-h)}{d} \right) \tag{15}$$

$$\left\langle E_z{}^2 \right\rangle = \left| \frac{t_p \cdot n_1 \sin(\theta)}{\hat{n}_3} \right|^2 \exp\left(-\frac{(z-h)}{d} \right) \tag{16}$$

The *x* and *z* directions lie in the plane of incidence with the *z* direction normal to the solid liquid interface. The *y* direction is perpendicular to the plane of incidence. The distance from the n_1, $\hat{n}_2$ interface is *z*, and the thickness of the second phase is *h*. The Fresnel transmission coefficients t_p and t_s are:

$$t_s = \frac{t_{s12} t_{s23} \exp(i\beta)}{1 + r_{s12} r_{s23} \exp(2i\beta)} \tag{17}$$

$$t_p = \frac{n_1 t_{p12} t_{p23} \exp(i\beta)}{\hat{n}_3\left[1 + r_{p12} r_{p23} \exp(2i\beta)\right]} \tag{18}$$

$t_{p,jk}$, $t_{s,jk}$, $r_{p,jk}$, and $r_{s,jk}$ are the Fresnel transmission and reflection coefficients for each planar phase boundary in the system

$$t_{s,jk} = \frac{2\xi_j}{\xi_j + \xi_k} \tag{19}$$

$$t_{p,jk} = \frac{2\hat{n}_k{}^2 \xi_j}{\hat{n}_k{}^2 \xi_j + \hat{n}_j{}^2 \xi_k} \tag{20}$$

$$r_{s,jk} = \frac{\xi_j - \xi_k}{\xi_j + \xi_k} \tag{21}$$

$$r_{p,jk} = \frac{\hat{n}_k{}^2 \xi_j - \hat{n}_j{}^2 \xi_k}{\hat{n}_k{}^2 \xi_j + \hat{n}_j{}^2 \xi_k} \tag{22}$$

β is defined as follows

$$\beta = 2\pi\xi_3 \frac{h}{\lambda} \tag{23}$$

3.3.2 Calculation of Time Averaged Mean Square Electric Fields

Accurate values for the complex refractive indices of D_2O and silicon are needed in order to calculate the mean square electric field strengths and are given in Table 2. The C_{14}TABr asymmetric stretch bands were integrated from 2800 cm^{-1} to 3000 cm^{-1}, the weighted average wavenumber of the integration region was 2910 cm^{-1}. The C_{14}TABr-d_{38} stretch bands were integrated from 2025 cm^{-1} to 2265 cm^{-1}, and the weighted average wavenumber of the integration region was 2159 cm^{-1}. The complex refractive index of D_2O at 2910 cm^{-1} and 2159 cm^{-1} was used in calculating the Gibbs Surface Excess for the C_{14}TABr and C_{14}TABr-d_{38}, respectively.[64]

Table 2. Refractive indices of D_2O and silicon, and weighted wavelength used in the calculation of the Gibbs surface excess for C_{14}TABr and C_{14}TABr-d_{38}.

Variable	C_{14}TABr	C_{14}TABr-d_{38}
$\tilde{\upsilon}$	2910 cm^{-1}	2159 cm^{-1}
λ	3.436 μm	4.362 μm
n_1 (silicon)	3.430	3.425
$\hat{n}_2 = \hat{n}_3$ (D_2O)	1.236 + 0.002i	1.399 + 0.014i

The three phase equations were programmed into Maple 7. Due to the large fluctuation of surfactant at the surface in the kinetic experiments and based on the finding of Nievandt and Citra the interface was treated as a two layer system, with $\hat{n}_2 = \hat{n}_3$, and $h = 0$. [8,49,56] The infrared absorption by the surfactant depends on the electric field strength, which decays exponentially as a function of distance, z, from the n_1 n_2 interface. Because we do not know the z dependence of the surfactant concentration, we calculated the electric field strength at z = 0 for surfactant adsorbed at the n_1 n_2 interface. A typical decay length of the evanescent wave is 140 nm, so this approximation is invalid when concentration fluctuations extend to distances greater than ~50 nm.

Calculated mean square electric field strengths in the x, y and z directions are given in Table 3. The Maple® worksheets used to determine the mean square electric fields are included in appendix A.

Table 3. Mean square electric field strengths in the x, y, and z directions calculated using the Hansen two phase model. Calculated values were used in determining the Gibbs surface excess for C_{14}TABr methylene stretch at 2910 cm^{-1} and C_{14}TABr-d_{38} methylene stretch at 2159 cm^{-1}.

MSEF Orientation	C_{14}TABr	C_{14}TABr-d_{38}
$\langle E_x \rangle^2$	1.670	1.638
$\langle E_y \rangle^2$	1.951	2.031
$\langle E_z \rangle^2$	2.159	2.307

Chapter 4 EXPERIMENTAL

4.1 REAGENTS & PURIFICATION METHODS

Tetradecyltrimethylammonium bromide (C_{14}TABr) from Sigma was recrystallized three times from acetone and a fourth time from absolute ethanol (the ethanol was vacuum distilled at room temperature). Perdeuterated tetradecyltrimethylammonium bromide (C_{14}TABr-d_{38}) (The Thomas Group, Oxford, UK) was used as received. According to the manufacturer the isotopic ratio was D:H = 98:2. From integration of the IR absorption in an ATR experiment, we find 97.5% D. Deuterium oxide was used as the solvent to avoid overlap of the methyl and deuterated methyl stretches with the water OH stretch and OH combination band, respectively. Deuterium Oxide (99.9%) was purchased from Cambridge Isotope Laboratories and distilled prior to use. Solutions were degassed and the pD was not altered with acids or bases, so the experimental results should be roughly comparable to those obtained in H_2O at pH 7. Potassium bromide from Aldrich was roasted at 300°C in air ~12 hours to eliminate organic impurities.

4.2 SILICA SURFACE PREPARATION

The native oxide layer of a silicon internal reflection element (IRE) (Wilmad, Buena, NJ) was cleaned by rinsing in absolute ethanol and scrubbing lightly with a cotton-tipped applicator. The IRE was rinsed in distilled, deionized water with a conductivity of 18.3 MΩ cm at 25 °C prepared by an EASYpure UV system (model D7401, Barnstead Thermolyne Co., Dubuque, IA) and then dried in a stream of ultra pure nitrogen. The optical faces of the IRE were treated with UV radiation from an UVP Pen Ray lamp (UVP Upland, CA) for 30 minutes at a distance of ~5 mm.[47,65] The IRE was sealed in the flow cell immediately following the UV treatment.

4.3 TRANSMISSION ABSORPTION COEFFICIENT OF C_{14}TABr SURFACTANTS

Sample spectra of the methyl and methylene stretching bands of the two C_{14}TABr surfactants[38,66,67] used in the study are given in Figure 11. The signal to noise level for one interferometer scan and for 256 scans are given beneath the stretch bands.

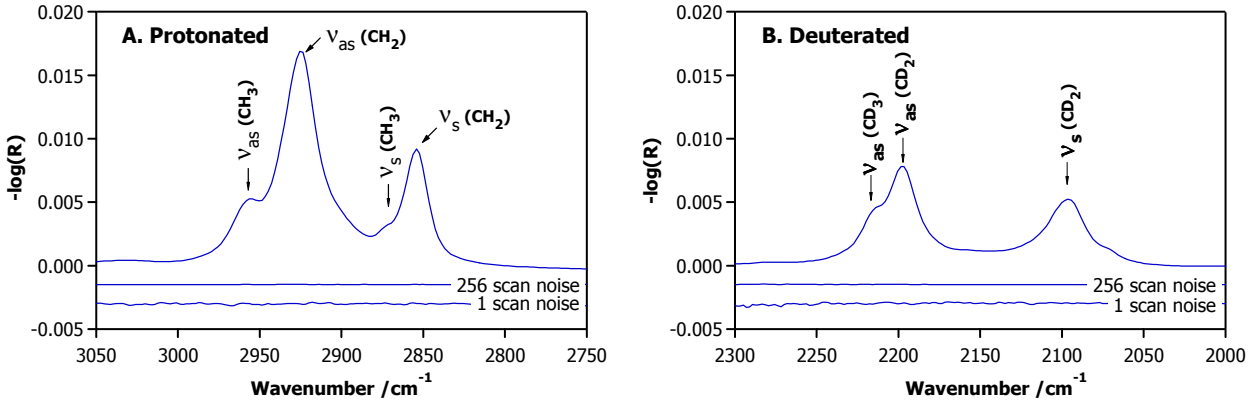

Figure 11. Sample spectra of A. C_{14}TABr B. C_{14}TABr-d_{38}. Noise levels for a single scan and 256 scans are demonstrated by the two spectra beneath the stretch bands, which were measured in the absence of surfactant.

4.3.1 Transmission Flow Cell Calibration

Molar absorption coefficients for the protonated and deuterated surfactants were determined using a transmission cell with a fixed path length of 104.2 microns. The path length was verified by counting the interference fringes of the empty cell.[68] See Figure 12.

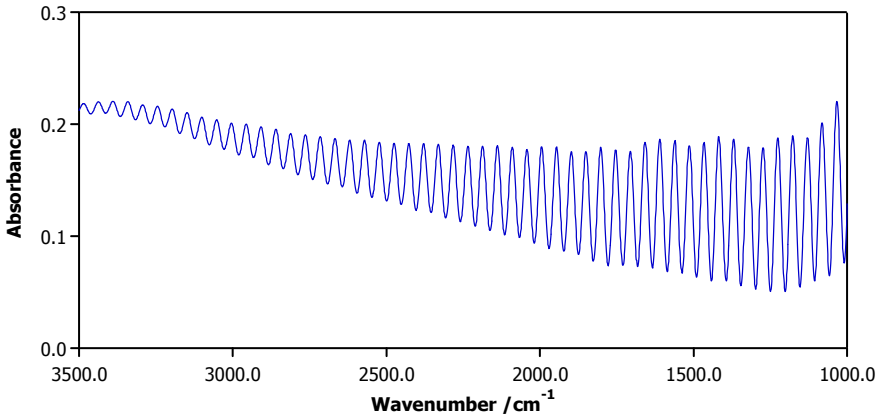

Figure 12. Interference fringe pattern used to calibrate the path length.

This process of calibrating the path length was repeated each time the transmission flow cell was used to determine a molar extinction coefficient.

The path length was determined using the following equation.[68]

$$b = \frac{N_{fringe}}{2n(\tilde{\upsilon}_2 - \tilde{\upsilon}_1)} \quad (24)$$

N_{fringe} is the number of interference fringes, and n is the refractive index of the sample within the cell, (in our case nitrogen was used, with n = 1.000). $\tilde{\upsilon}_1$ and $\tilde{\upsilon}_2$ are the wavenumber in reciprocal meters of the interference fringe maxima. Wavenumbers of fringe maxima were determined using the Omnic peak pick routine.

4.3.2 Protonated C_{14}TABr

The molar absorption coefficient for C_{14}TABr was measured in D_2O at multiple concentrations similar to those used in the ATR-FTIR kinetic experiments. A linear regression of integrated absorbance (integrated from 2800 cm^{-1} to 3000 cm^{-1}) with respect to concentration in mol m^{-3} gave an absorption coefficient of 3.6167×10^6 cm^{-1} $Molar^{-1}$ m^{-1}.

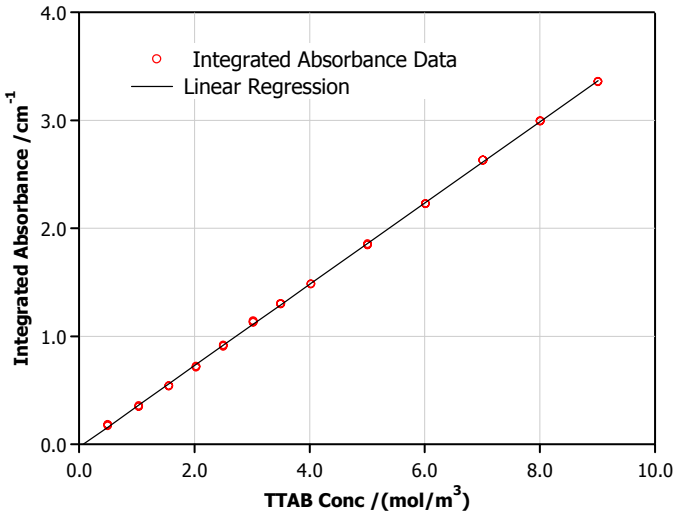

Figure 13. Data used to determine the integrated absorption coefficient for C_{14}TABr. A linear regression of the data gives ε = 3.6167 × 106 cm^{-1} $Molar^{-1}$ m^{-1}.

4.3.3 Deuterated C_{14}TABr

The integrated molar extinction coefficient of C_{14}TABr-d_{38} was measured in water, but water has a combination band at 2500 cm^{-1} that interferes with the stretching bands of the deuterated surfactant. A hydrogen bonding solvent (methanol) was chosen to provide a similar environment to D_2O. An absorption coefficient for C_{14}TABr-d_{38} was determined by scaling the C_{14}TABr absorption coefficient measured in D_2O by the ratio of C_{14}TABr-d_{38} to C_{14}TABr measured in methanol.

C_{14}TABr asymmetric stretch regions were integrated from 2800 to 3000 cm^{-1} and C_{14}TABr-38 was integrated from 2025 to 2265 cm^{-1}. Perdeuterated methanol (methanol-d4) was used as a solvent for the protonated surfactant, and methanol as a solvent for the C_{14}TABr-d_{38}. The integrated absorption coefficients for C_{14}TABr-d_{38} and C_{14}TABr in methanol are 1.7969×10^6 cm^{-1} $Molar^{-1}$ m^{-1} and 3.8501×10^6 cm^{-1} $Molar^{-1}$ m^{-1} respectively. The molar absorption coefficient of 1.6880×10^6 cm^{-1} $Molar^{-1}$ m^{-1} for C_{14}TABr-d_{38} in D_2O was calculated by scaling the C_{14}TABr absorption coefficient in D_2O by 0.4667.

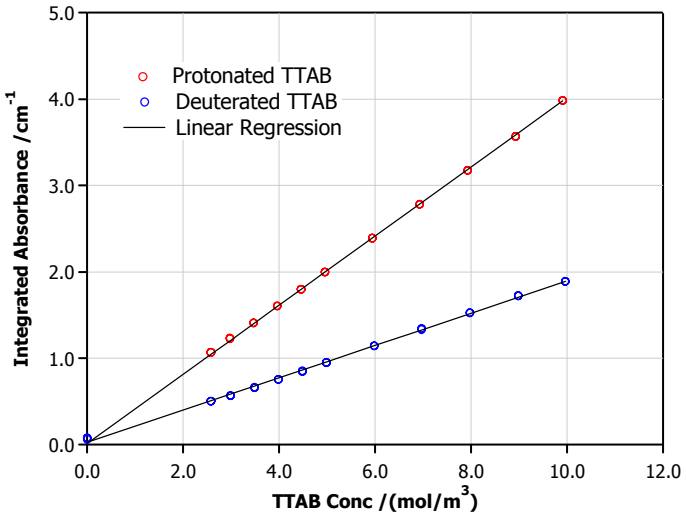

Figure 14. Data used to determine the integrated absorption coefficients for C_{14}TABr and C_{14}TABr-d_{38} in methanol. Linear regression of the data gives molar absorption coefficients of 3.8501×10^6 and 1.7969×10^6 cm^{-1} $Molar^{-1}$ m^{-1} respectively.

4.4 ATR-FTIR

4.4.1 Instrumentation

Infrared spectra were collected using a Nicolet Nexus 670 Fourier transform infrared spectrometer (Madison, WI) equipped with a liquid nitrogen cooled MCT-A detector, a Ge on KBr beamsplitter, and a vertical variable-angle ATR accessory from CIC Photonics (Albuquerque, NM). Dry nitrogen was used as a purge gas. The custom silicon IRE , $80.0 \times 8.0 \times 3.20$ mm, was a single pass 45-degree parallelogram crystal.

The IRE was sandwiched between two Teflon flow cells fitted with Kalrez® 8201 o-rings. The cell design allows circulation of fluid across the full length of both optical faces, and solutions contact only glass, Teflon®, the Kalrez® o-rings (Dupont Dow Elastomers), and the IRE surface.

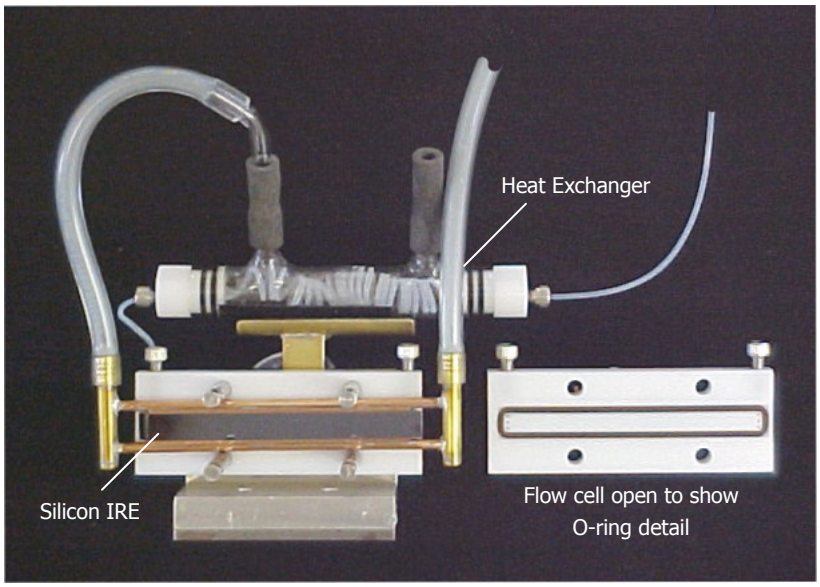

Figure 15. Attenuated Total Internal Reflection apparatus. The ATR flow cell used is shown with the solution heat exchanger, and IRE heat exchanger. The front half of the flow cell has been removed to show the IRE crystal and o-ring detail.

The cell dimensions are 0.3 mm thick × 7.5 mm wide × 78.5 mm long. Solutions were circulated using a peristaltic pump with a rigid PTFE-tubing pump head (Masterflex), and were isolated from the ambient atmosphere. A pump head that utilized elastomer tubing resulted in contaminated data, regardless of the tubing formulation. The flow cell was thermostated to minimize temperature-induced fluctuation of the OD stretch of D_2O at 2500 cm^{-1}. This was accomplished by circulating water through a copper heat sink cemented to the non-optical faces of the IRE. The temperature of the surfactant solutions prior to entry to the cell was controlled by a heat exchanger at the cell entrance.

All experiments were performed at 25 ± 0.2°C, except for a low temperature kinetic experiment, which was conducted at 6.0 ± 0.3°C. The temperature was controlled using a thermostated water bath (VWR) and measured at the outlet and inlet to the cell.

4.4.2 Cleaning Procedure

In order to avoid contamination from oils and plasticizers, the Teflon flow cell and all other hardware that came in contact with surfactant solutions were cleaned before each experiment. Teflon tubing was washed with Liqui-Nox detergent solution, rinsed with Nano-pure water and then blown dry with nitrogen. Glassware was washed with Liqui-Nox solution, rinsed in Nano-pure water, soaked in warm base bath, rinsed in ultra-pure water, and then dried in an oven at 150°C. The flow cell, o-rings, and all fittings were sonicated in a solution of C_{12}TABr for 15 minutes, rinsed in Nano-pure water, sonicated in Nano-pure water for 15 minutes, and then blown dry with nitrogen. Cleaning

and assembly was done while wearing gloves, and final assembly of the cell was done in a laminar flow cabinet.

4.4.3 Spectrometer Polarization Ratio

The evanescent penetration depth into the surfactant solution is polarization dependent. The penetration depth is calculated separately for s and p-polarized infrared radiation and a weighted mean of the two polarizations is used in determining the effective path length, $b_{eff,unp}$. The polarization ratio, PR, is unique to the spectrometer (detector and optics within the FTIR bench) and is wavelength dependent. The *s* and *p*-polarized absorbance spectra of an isotropic sample were measured with respect to an unpolarized background spectra taken with no sample present.

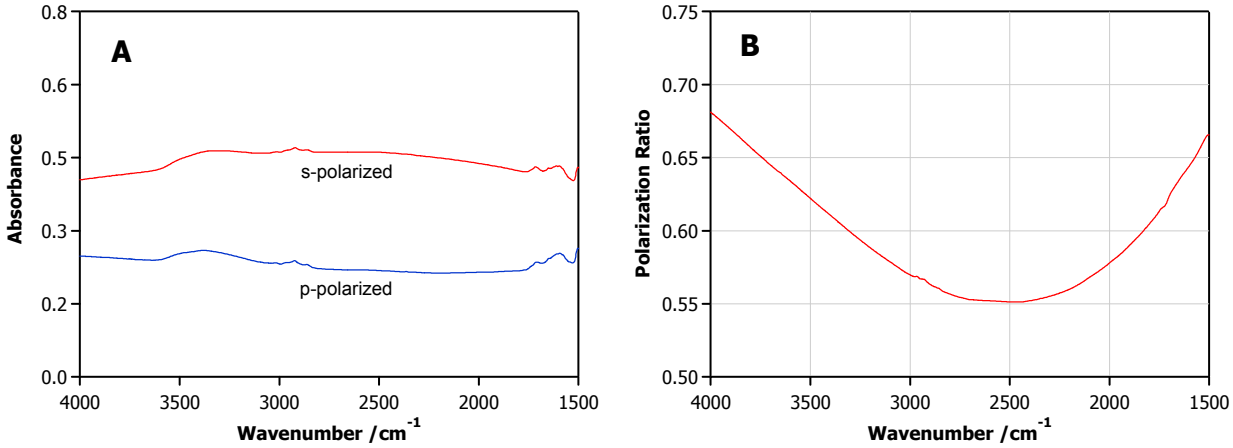

Figure 16. A. *s* and *p*-polarized absorbance spectra of the empty, clean silicon ATR crystal. B. Wavelength dependent polarization ratio calculated using equation 25.

The wavelength dependent polarization ratio[62,63] PR can be calculated from the *s* and *p*-polarized absorbance spectra $A_{s(\tilde{\upsilon})}$ and $A_{p(\tilde{\upsilon})}$ and the polarizer percent "leakage" L, (0.03 at 3000 cm^{-1}).

$$PR(\tilde{\upsilon}) = \left[\frac{1 - L \cdot 10^{(A_s(\tilde{\upsilon}) - A_p(\tilde{\upsilon}))}}{10^{(A_s(\tilde{\upsilon}) - A_p(\tilde{\upsilon}))} - L} \right] \tag{25}$$

The wire grid polarizer used was a Molectron IGP-228 (0.25 mm spacing on a BaF_2 substrate). The polarizer has an efficiency of 98% @ 3.9 µm and 93% at 1.5 µm. The spectrometer had polarization ratios of 0.5655 and 0.5633 at 2910 cm^{-1} and 2159 cm^{-1} respectively.

4.4.4 Determination of Internal Reflection Number

The number of internal reflections obtained for a particular internal reflection element can be calculated based on the element dimensions and the entrance angle of the beam. The number of internal reflections that actually "sensed" the solution was verified using a method similar to Sperline's for calibrating ATR flow cells that utilize a cylindrical element.[69] A solution of 273.13 mM

D_2O in H_2O was used as a calibration standard. The OD stretch of the D_2O had an integrated -log(R) value of 3.554 and an absorbance of 60.770 in ATR and transmission mode, respectively. The peak was integrated from 2000 to 2740 cm. The calibration solution had to be concentrated enough to give a sizable signal in the ATR, without an absorbance in excess of ~0.75 in transmission mode.

$$N = \frac{-\log(R)\cdot b}{A\cdot b_{eff,unp}} \tag{26}$$

N is the number of internal reflections, -log(R) the integrated ATR spectra of the calibration solution, A is the transmission absorbance, and b is the transmission path length of 104.2 µm. The unpolarized effective path length, $b_{eff,unp}$ is calculated using equations 12 and 13. An incident angle of 60.0 degrees gives a $b_{eff,\ unp}$ value of 279.5 nm. The number of solution sensing internal reflections was 22.09. The angle corresponding to an even number of internal reflections can be determined experimentally by varying the incident angle, until the throughput passes through a maximum.

4.5 EQUILIBRIUM EXPERIMENTS

4.5.1 Protonated C_{14}TABr Isotherm

Prior to an experiment, the detector was cooled to liquid nitrogen temperatures and the interferometer was aligned. The ATR flow cell was placed in the spectrometer bay and aligned. Background spectra were taken with no solution in the flow cell. The flow cell was then connected to the recirculating water bath (VWR) and the D_2O reservoir. Freshly distilled and degassed D_2O was pumped across the crystal surface at a rate of 2.0 ml/min. The interferometer and equipment were left running and allowed to equilibrate for 12 hours before recording any measurements. Experiments were started after sample spectra of D_2O referenced to a D_2O background were linear, with minimal fluctuation in the D_2O stretching region. All sample spectra were 128 co-added scans collected in triplicate and referenced to pure D_2O. Spectra were collected automatically using Omnic Macro Basic software. C_{14}TABr titrant was added to a recirculating C_{14}TABr solution using a computer controlled peristaltic pump and Windows® Linkable Instrument Network software. The surfactant concentration was stepped from zero to 7.0 mM in 22 intervals and allowed to equilibrate for 50 minutes before collecting sample spectra.

Spectrometer settings used for isotherm experiments are as follows: mirror velocity 0.9494 cm/s, 2 cm^{-1} resolution, no zero filling, gain setting of 1.0, -log(R) format, and Happ Genzel apodization.

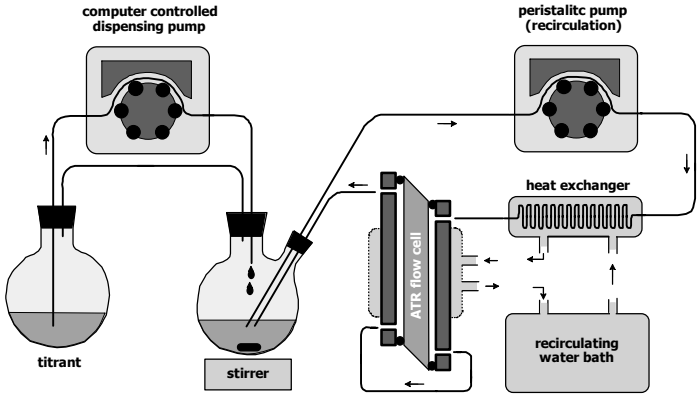

Figure 17. Experimental set-up used for equilibrium experiments. Dispensing of liquid is computer controlled. The solution is temperature controlled by the heat exchanger before flowing into the cell. The entire system is isolated from the atmosphere to prevent water and gasses from influencing the ATR spectra.

4.5.2 Isotherm of a 1:1 Mole Ratio Mixture of C_{14}TABr and C_{14}TABr-d_{38}

One concern with using deuterated surfactant is that the 15% increase in mass of the $C_{14}TA^+$ ion would adversely influence the kinetics or thermodynamic behavior of the molecule.[46,70] The ideal C_{14}TABr analogue would have identical chemical and physical properties. A combined isotherm experiment was conducted with a 1:1 mole ratio of C_{14}TABr and C_{14}TABr-d_{38} to determine if one of the surfactants would adsorb preferentially. The results show that the surface aggregates are composed of 53% protonated to 47% deuterated surfactant. C_{14}TABr-d_{38} does not behave identically to C_{14}TABr, but the behavior is satisfactory. A better analogue would have been $(CH_3)_3N^+(CD_2)_{13}(CD_3)$. The protonated head group would be identical to C_{14}TABr and the deuterated tail would serve as the spectroscopic probe.

4.6 KINETIC EXPERIMENTS

The procedure was similar to that used in the isotherm experiments, except for a 3 hour equilibration period. The procedure used to observe adsorption, exchange, and desorption of C_{14}TABr from the surface is as follows. Pure D_2O or KBr solutions were used to establish the initial baseline. The solution input was switched to C_{14}TABr solution, to C_{14}TABr-d_{38} solution, back to C_{14}TABr solution, and then to D_2O or KBr solution. Spectrometer settings for the kinetic experiments were the same as equilibrium experiments with the following exceptions: mirror velocity was 1.2659 cm/s, and resolution was set to 4 cm^{-1}. These settings were selected because they gave the greatest signal to noise ratio in the least amount of time.

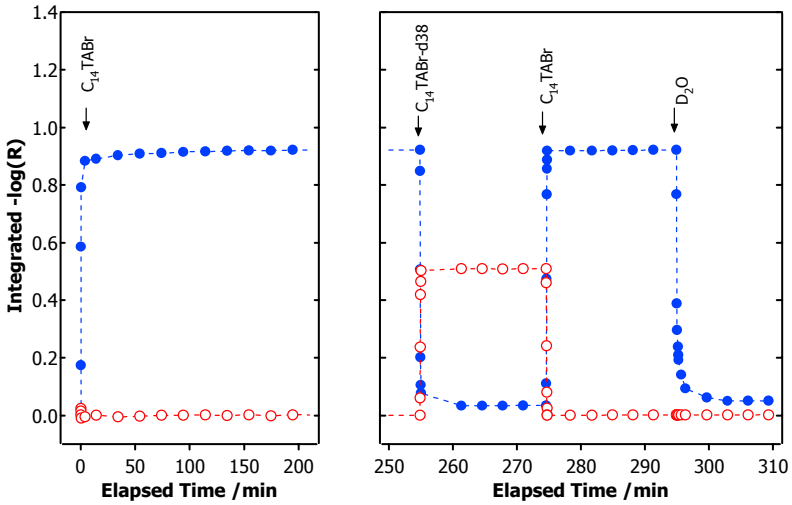

Figure 18. Overview of typical experiment showing integrated -log(R) and surface excess for C_{14}TABr (●) C_{14}TABr-d_{38} (○). Γ* is the Gibbs surface excess calculated without subtracting the contribution from surfactant in bulk. The starting state is pure D_2O, the arrows show where the solution was changed.

4.6.1 Concentration "Jump" Methods

A limiting factor in the kinetic resolution was transport (both forced convection and diffusion) of the new solution to the solid-liquid interface though the stagnant layers near the optical surface. This time was reduced by separating the old and new solutions with a small air bubble (~0.25 ml). When the bubble passed through the cell, it spanned the entire width and thickness of the cell, and therefore provided a more sudden change in solution concentration by exchanging solution very close to the optical surface. We could also monitor the passage of the bubble through the ATR cell using the FTIR spectrometer. In some cases, the bubble penetrated the evanescent zone (~200 nm thick). In these cases, the passage of the bubble could have altered the surface structure. In other cases, the bubble did not penetrate the evanescent zone and it was safe to assume that it provided solution exchange via forced convection without immediately disturbing the surface film. Note that the solution flows *ahead* of the bubble in Figure 19 B.

Experiments utilizing a bubble and those not utilizing a bubble are labeled "bubble" and "no-bubble" respectively. The row of three holes used at the cell inlet and outlet was a poor design (see Figure 19 A), as the holes cause inefficient exchange of solvent. A continuous slot would facilitate a more abrupt change between solutions for the "no-bubble" experiments.

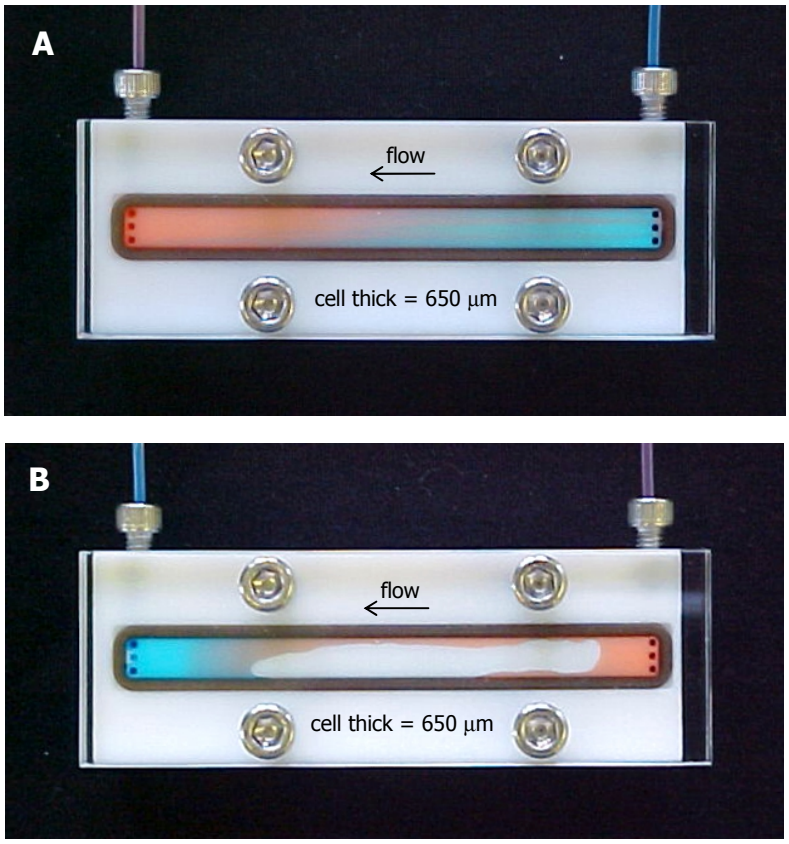

Figure 19. Flow cell interior showing A. "No-bubble" method. B. "Bubble" method used to conduct "concentration jump" experiments. Flow direction is from right to left. Dye is used to visualize the flow pattern within the cell.

The pump flow rate was set at 7.5 ml/min for the initial 2 ml of solution, and reduced to 2.0 ml/min there after.

4.6.2 Procedure

Adsorption of $C_{14}TABr$ The initial $C_{14}TABr$ solution was allowed to adsorb for three hours. One-scan spectra were collected at 2.2 second intervals during the first minute of adsorption, eight-scan spectra were collected at six second intervals for the next 2.5 minutes and 256-scan spectra at 10 minute intervals for a period of 200 minutes. Three 128-scan background spectra were taken after the equilibration period of 2.5 hours with $C_{14}TABr$ adsorbed to the SiO_2 surface.

Exchange from $C_{14}TABr$ to $C_{14}TABr$-d_{38} to $C_{14}TABr$ After the initial adsorption of protonated surfactant, the solution was switched to deuterated surfactant at the same concentration. One scan spectra were collected at 2.2 second intervals for the first minute, and 8-scan spectra were collected at six second intervals for the next two minutes. Five 256-scan spectra were collected over a period of 16 minutes. The $C_{14}TABr$-d_{38} solution was switched back to $C_{14}TABr$ and the same scan protocol was followed.

Desorption of $C_{14}TABr$ $C_{14}TABr$ solution was switched to pure D_2O or a deuterium oxide solution of KBr. Single scan spectra were collected at 2.2 second intervals for the first 2 minutes and 256-scan spectra were collected at 3.2 minute intervals for another 32 minutes.

4.7 AFM FORCE CURVE FREQUENCY EXPERIMENTS

AFM force curves in $C_{14}TABr/D_2O$ were measured using a Digital Instruments Nanoscope III AFM and a silicon nitride cantilever and tip with a nominal spring constant of 0.24 Nm^{-1}. The range of the force curves was 300 nm.

4.8 ATR-FTIR DATA REDUCTION

All spectra were auto named and saved during the experiments. After completion of an experiment the spectra were converted from the proprietary Nicolet format to comma delimited values and imported into a Mathcad® worksheet. Mathcad 8.0 service pack 3 was used to baseline correct and integrate peak areas of all spectra using a common set of criteria. Protonated symmetric and asymmetric stretch bands were integrated from 2800 to 3000 cm^{-1}. Deuterated symmetric and asymmetric stretch bands were integrated from 2025 to 2265 cm^{-1}. In order to quantitate adsorbed $C_{14}TABr$-d_{38} in the kinetic, "no-bubble" experiments, all spectra involving exchange of protonated and deuterated surfactant were referenced to a background spectrum taken after the initial adsorption of $C_{14}TABr$ had reached equilibrium. This eliminated the large negative peak from desorption of D_2O that occurred when the initial $C_{14}TABr$ adsorption took place, see Figure 22.

In the case of equilibrium experiments, the Gibbs surface excess was calculated using equation 9a, because the surfactant concentration in the bulk was known. Gibbs surface excess values for the kinetic experiments were calculated from equation 9b and are labeled as Γ^* to distinguish them from the equilibrium experiments. No correction is made for absorbance in the bulk medium, because there was no way to accurately determine the bulk concentration. This approximation may give Γ^* values ~9% greater than Γ.

Chapter 5 RESULTS AND DISCUSSION

5.1 THREE KINETIC REGIMES OF INTEREST

Figure 20 shows the adsorption isotherm for $C_{14}TABr$ in D_2O at neutral pD. The break in the curve shows that the cmc of $C_{14}TABr$ in D_2O is about 3.2 mM. The absence of a maximum in Γ near the cmc is consistent with the absence of surface active impurities in our system. For equilibrium measurements (Figure 20) the contribution from analyte in bulk was subtracted to obtain the Gibbs surface excess using equation 9a.

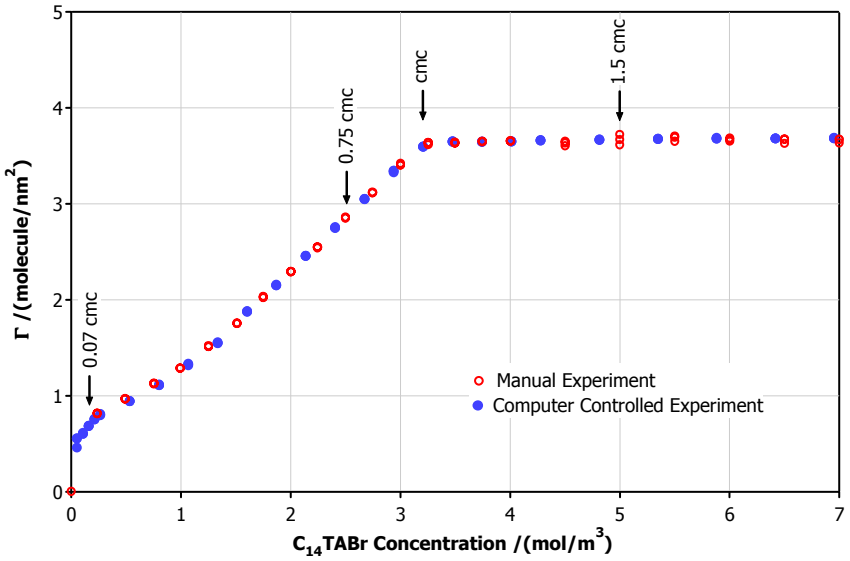

Figure 20. Adsorption isotherm of $C_{14}TABr$ on the native SiO_2 surface of the silicon ATR element. All samples were degassed, and the pD ~7, no adjustment was made to the natural pD. Solid markers are data collected using the automated system. Open symbols are data collected manually.

Three regions of the isotherm were explored in the kinetic experiments: one tenth the cmc, slightly below the cmc, and above the cmc. The three regions were chosen because different aggregate states were present. At about one tenth of the cmc, only monomers are present in solution. Some surfactant has adsorbed at the silica surface, but no distinct aggregate structure exists. Just below the cmc fairly well characterized aggregates have formed at the silica surface and the bulk solution contains monomers. Above the cmc, micelles and monomers are present in solution and well characterized aggregates are found at the silica surface.[31]

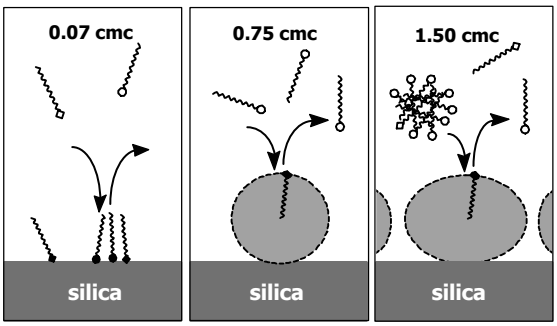

Figure 21. Schematic of the three exchange regimes. At 0.07 cmc the solution contains monomers, and the isotherm is consistent with small aggregates on the surface. At 0.75 cmc, the solution contains monomers and the isotherm is consistent with micelles at the surface. At 1.5 cmc, the solution contains monomers and micelles, and the micelles have a larger aggregation number.[31]

5.2 KINETICS OF ADSORPTION, EXCHANGE, AND DESORPTION

Figure 22 shows a time-series of spectra for a typical experiment, in this case the replacement of C_{14}TABr-d_{38} aggregates by C_{14}TABr is complete within 9 seconds. Spectra show that the quantity of water in the evanescent zone is constant during the exchange, and that after surface exchange occurs, the solution can be exchanged back to obtain the original surface spectrum.

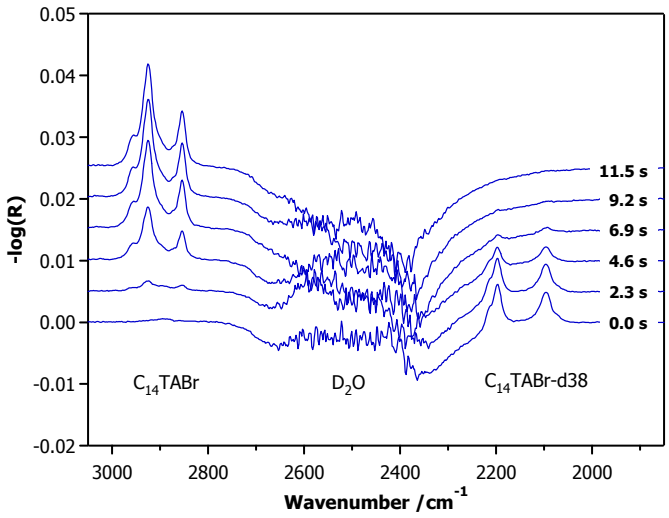

Figure 22. Exchange of C_{14}TABr-d_{38} for C_{14}TABr in the evanescent zone. The signal includes a contribution of < 9% from surfactant in bulk. The kinetics series is referenced to a pure D_2O background. Note the desorption of D_2O during the initial adsorption of C_{14}TABr.

Exchange experiments at 1.5 cmc, 0.75 cmc, and 0.07 cmc are shown in Figures 23, 24, and 25. The principle result is that the exchange of D_2O for surfactant or surfactant for surfactant are both very fast, whereas exchange of surfactant for D_2O is slower. The fast rate of adsorption (equilibrium within 10 seconds) is similar to that observed previously by Atkin et al. [29] using reflectometry (~20 s), and casts some doubt on the very slow adsorption rates (minutes to hours) that have been observed in other work.[42,43,45] The novel aspect of the present work is our observation of the very rapid exchange of one surfactant molecule for another at the surface.

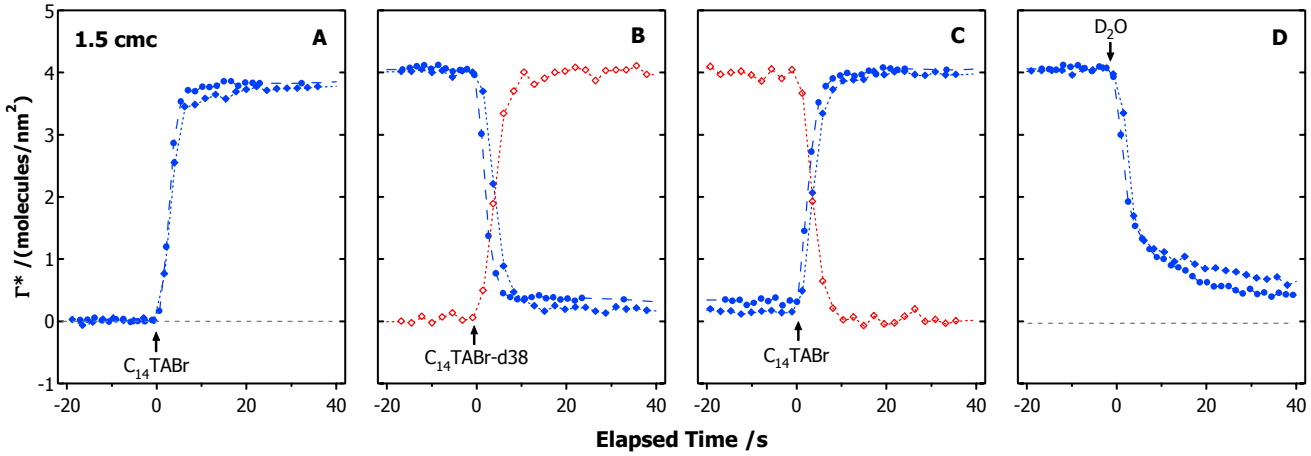

Figure 23. Kinetics of C_{14}TABr at 1.5 cmc at 25.0 Celsius for the bubble (circles), and no bubble experiments (diamonds). A. Adsorption. B. Exchange of C_{14}TABr (solid marker) to C_{14}TABr-d_{38} (open marker). C. Exchange of C_{14}TABr-d_{38} to C_{14}TABr. D. Desorption of C_{14}TABr. Dashed lines are added to guide the eye.

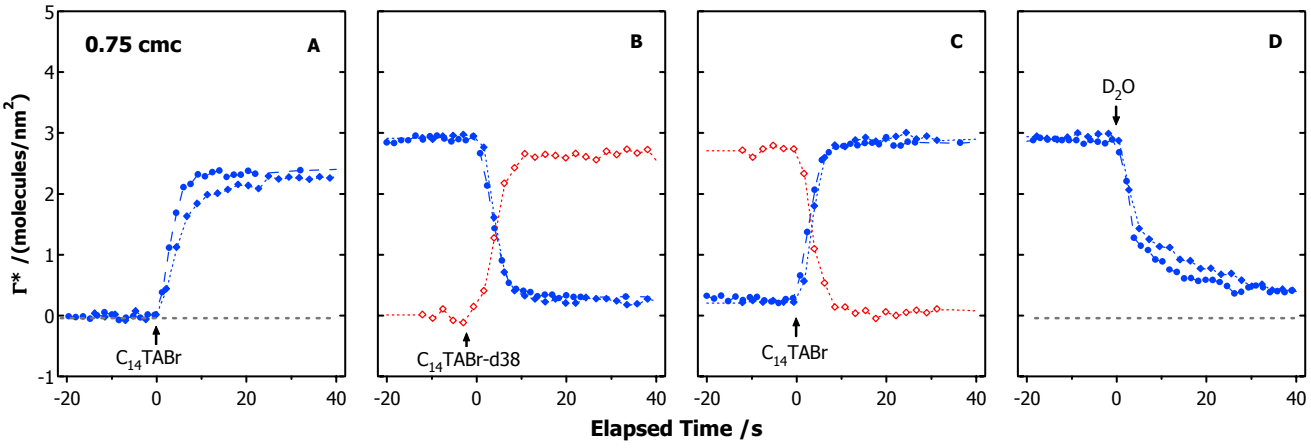

Figure 24. Kinetics of C_{14}TABr at 0.75 cmc at 25.0 Celsius for the bubble (circles), and no bubble experiments (diamonds). A. Adsorption. B. Exchange of C_{14}TABr (solid marker) to C_{14}TABr-d_{38} (open marker). C. Exchange of C_{14}TABr-d_{38} to C_{14}TABr. D. Desorption of C_{14}TABr. Dashed lines are added to guide the eye.

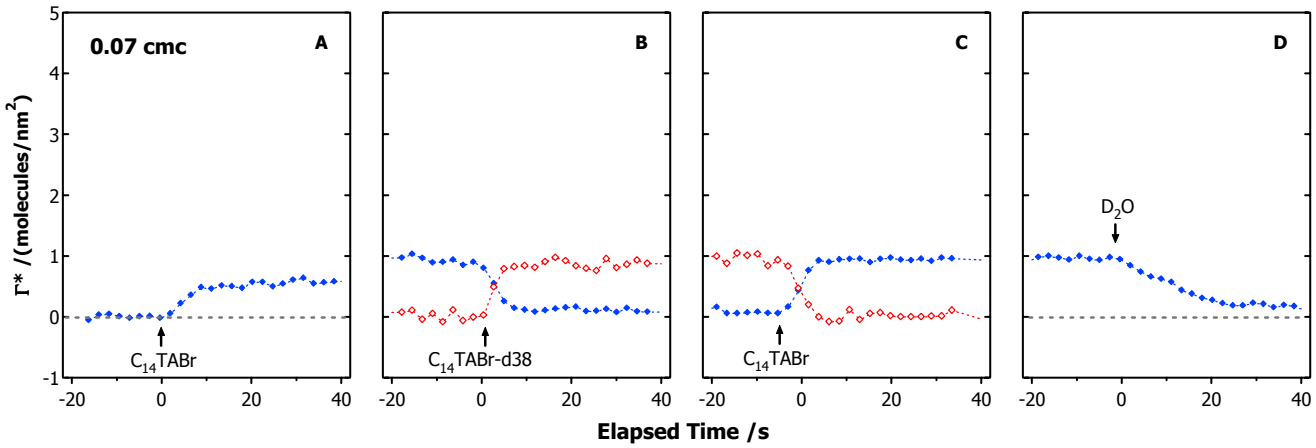

Figure 25. Kinetics of C_{14}TABr at 0.07 cmc at 25.0 Celsius for the no bubble experiments (diamonds). A. Adsorption. B. Exchange of C_{14}TABr (solid marker) to C_{14}TABr-d_{38} (open marker). C. Exchange of C_{14}TABr-d_{38} to C_{14}TABr. D. Desorption of C_{14}TABr. Dashed lines are added to guide the eye.

Figures 23-25 show that this exchange is much faster than the final stages of replacing adsorbed surfactant with D_2O. The rate of exchange of surfactant between the bulk and the surface depends on the transport rate to the surface, as well as rates of processes in the diffuse double-layer and the Stern layer. To arrange for more rapid delivery of surfactant to the surface, a bubble was used to separate the old and new solutions during exchange. The passage of the bubble through the cell swept out more of the old solution and provided a moving boundary condition nearer to the interface than would occur simply by exchanging liquids. The transport time to bring new material to the surface is shorter under this condition than for a normal exchange of solution. Experiments with bubbles in 0.07 cmc caused a large decrease in the water signal, which made baselining of the methylene stretch difficult, and left us suspicious that the bubble may have touched the reflection element. This is consistent with a tails-out surfactant conformation as shown in Figure 21. Therefore, the kinetic data at 0.07 × cmc is not presented here. The bubble experiments demonstrate a faster rate of all exchange processes, an indication that our no-bubble experiments are transport limited.

At 0.75 cmc, most of the adsorption occurs in a short period of time, but a small amount of additional adsorption did occur over a long period of time (observe the break between A and B in Figure 24 and 25). The profile of this additional adsorption was variable in our experiments and will not be considered further. Neglecting this complication, the data shows that the time to reach at least 80% adsorption is similar at 0.07, 0.75 and 1.5 × cmc, so the data does not show any special role for micelles in speeding adsorption as reported by Velegol et al. Likewise, the same amount of time was required to exchange one surfactant for another over a wide range of bulk and surface concentrations. The data show no special role for micelles in altering the kinetics of exchange, but there is a possibility that such an effect might be resolved if a way is found to produce a more rapid perturbation from equilibrium.

The desorption of surfactant is slower, which allows us to resolve the desorption profile; the relevant data from Figures 23-25 is replotted in Figure 26. At 1.5 cmc a two stage adsorption is observed: the first 50-60% of the surfactant is removed very quickly and the remaining ~1.2 molecules/nm^2 desorbs at a slower time rate. Starting from a lower concentration (0.75 cmc or 0.07 cmc) produces the same result, a rapid loss of surfactant in the first few seconds followed by a slower loss of the remaining ~1.2 molecules/nm^2.

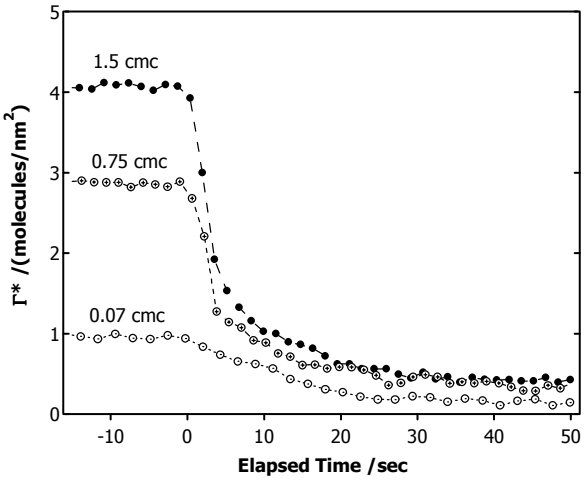

Figure 26. Desorption of C_{14}TABr by pure D_2O at 25.0 Celsius at three surface excess values, 1.5 cmc (●), 0.75 cmc (⊕), and 0.07 cmc (ʘ). Lines are a guide to the eye.

These two rates imply that the there are two environments for the surfactant: a strongly bound and a more weakly bound state. A reasonable hypothesis is that the weakly bound state consists of those molecules held by hydrophobic association of the alkyl chains, and that the strongly bound state is those molecules held to the silica by electrostatic forces. The surface density at which the strongly bound material is found in a desorption experiment is greater than the surface density at the top of the sudden rise in the adsorption isotherm (~0.8 molecules/nm^2). This is not completely surprising, it merely suggests that the addition of extra surfactant causes more surfactant to bind electrostatically (by displacing protons from the surface.) There is ample evidence for charge regulation by quaternary ammonium surfactants on silica.[71]

It is interesting that the exchange of surfactant for water is so much slower than the exchange of surfactant for another surfactant molecule (In Figures 24 and 25, compare B or C to D). After the first part of the adsorbed micelle has desorbed, the remaining adsorbed aggregate passes through an aggregation number or state, which experiences a big barrier to further desorption.

5.3 INFLUENCE OF SALT ON ADSORPTION AND DESORPTION

To test whether the activation barrier to desorption is electrostatic, the surfactant was desorbed with KBr solutions. To facilitate comparison of results for exchange with C_{14}TABr-d_{38}, we used the same concentration of salt as surfactant. Figure 27 shows that the rate of desorption is much greater in salt solution, and is similar to the rate in C_{14}TABr-d_{38}. This supports the hypothesis that an electrostatic force is important in the rate determining step during desorption.[72]

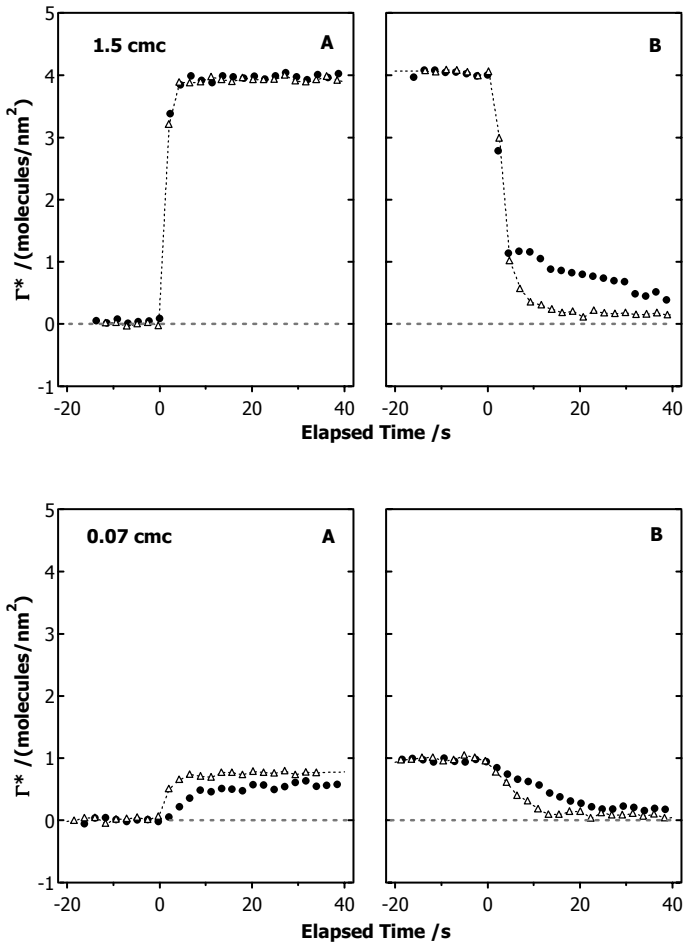

Figure 27. Influence of KBr on the adsorption and desorption of C_{14}TABr from silica surface at 25.0 Celsius. A. The circulating solution was changed from D_2O to C_{14}TABr (circles), and from a KBr solution to C_{14}TABr (triangles). B. Desorption of surfactant by D_2O (circles), and KBr solutions (triangles). The surfactant was allowed to equilibrate for 3.5 hours prior to desorption. Dashed lines are a guide to the eye.

Silica is negatively charged in water and is made positive by adsorption of surfactant, so desorption below the point of zero charge occurs against an electrical potential. Adsorption of K^+ ions in the salt (exchange of K^+ for $C_{14}TA^+$) should reduce the electrostatic barrier to desorption by reducing the surface potential and the Debye-length. In a pure D_2O or H_2O solution, the only cations available to

prevent the build-up of a negative potential are the very dilute protons. The data show a rapid adsorption followed by a slower adsorption. Based on the hypothesis that the slow approach to equilibrium resulted from a slow surface rearrangement involving protons, the silica surface was pretreated with KBr solution to remove protons, then displaced the KBr solution with surfactant solution. In this experiment, the aim was to displace H^+ with K^+ before the surfactant is present, but there is no K^+ present in solution after the exchange. This removes the possible rate enhancing effect of long-range electrostatic screening on the rate of surfactant adsorption. At 0.07 cmc the adsorption is distinctly faster when the surface is pretreated with K^+, which is consistent with the hypothesis of H^+ desorption being the limiting step. Above the cmc, the data show no change (the rate is already at our resolution), and the results at 0.7 cmc were too variable to reach a conclusion.

5.4 Low Temperature Studies

The surfactant exchange processes was monitored at 6.3°C and 0.75 cmc. 6.3°C is about 1°C above the freezing point of D_2O and about 8°C below the Krafft temperature of C_{14}TABr. (The Krafft temperature in D_2O was 14.4°C). Some earlier studies of surfactant adsorption and desorption reported slow rates that were performed on surfactants near the Krafft temperature (e.g. C_{16}TABr at 20–25°C) and we were curious to see whether the slow rates correlated with an experimental temperature below the Krafft temperature. Figure 28 shows that the kinetics of C_{14}TABr exchange below the Krafft temperature are similar to the kinetics above the Krafft temperature.

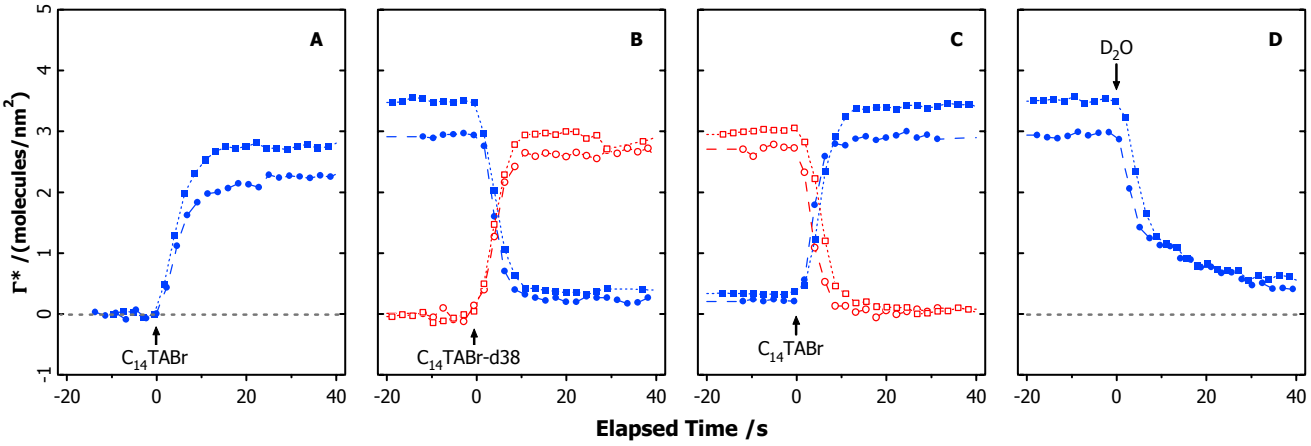

Figure 28. Kinetics of C_{14}TABr at 0.75 cmc at 25.0 Celsius (circles) and at 6.0 ±0.3 Celsius (squares) using the "no-bubble" method. A. Adsorption. B. Exchange of C_{14}TABr (solid marker) to C_{14}TABr-d_{38} (open marker). C. Exchange of C_{14}TABr-d_{38} to C_{14}TABr. D. Desorption of C_{14}TABr. Dashed lines are added to guide the eye.

There is very little change is adsorption or surfactant– surfactant exchange rates (as expected for a 19° Celsius temperature change in a transport-limited experiment) and slight slowing of desorption (as expected if the desorption is electrostatically activated). Surprisingly, we are able to resolve a large increase in surface excess for the lower temperature, which is perhaps related to a decrease in solubility of surfactant in bulk solution. The asymmetric CH stretch mode peak is located at 2924.4 cm^{-1} for the 6.0 Celsius experiment, and at 2925.2 cm^{-1} for the same experiment at 25.0 Celsius. The shift to lower wave number could be related to a change in surface aggregate structure.

5.5 WAVENUMBER STUDIES

The asymmetric stretch mode frequency was monitored during the adsorption and desorption process. Although wavenumber is not a definite indicator of the surfactant environment, the control experiments (Figure 29 A) show that the frequency moves back though the same frequencies observed during the equilibrium adsorption experiment. One might expect that if whole micelles were desorbing, the amount adsorbed would drop while the frequency would remain the same, but the data is not consistent with this process.

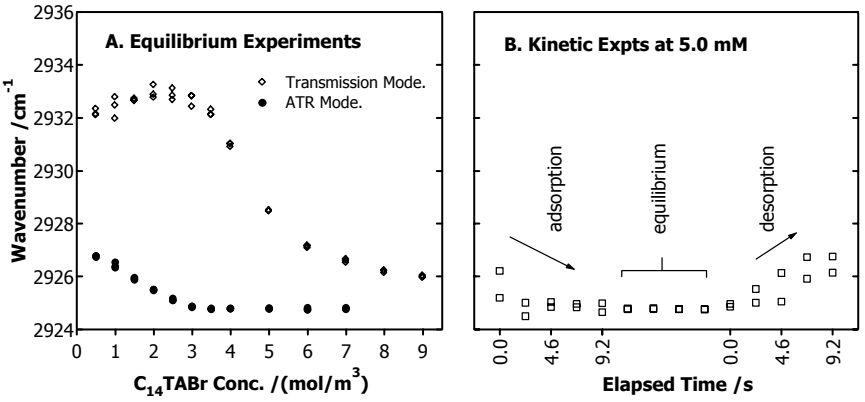

Figure 29. Methylene asymmetric stretching mode wavenumber. A. Wavenumber with respect to concentration for equilibrium processes, (diamonds) transmission absorption coefficient, and (circles)adsorption isotherm. B. Wavenumber of adsorbing, equilibrated, and desorbing surfactant in kinetic experiments.

5.6 ATOMIC FORCE MICROSCOPE (AFM) EXPERIMENTS

The slow rate of perturbation from equilibrium that was available by changing the concentration in the ATR-IR experiments led us to seek a faster way of perturbing the adsorbed structure. We also performed AFM experiments in which we measured the frequency dependence of the force required to displace a layer of surfactant at 1.5 cmc from the surface of silica. (The adsorbed surfactant forms a barrier to approach of the AFM tip). In this case, a mechanical force is applied to displace the surfactant rather than the chemical force (dilution) used in the ATR-IR experiments. The value of

comparison to AFM experiments of this type is diminished because we do not know the mechanism of displacement of surfactant by the AFM tip. Because the load applied by the AFM tip is not homogeneous across the surface, the surfactant could be displaced into solution (as in the ATR-FTIR experiments), or pushed across the interface. Also, because the zero of separation between the tip and sample is not known, the results may be showing displacement of only part of the surfactant film.

The results are shown in Figure 30. Even at repeat approach rates as high as 56 Hz, the surfactant is able to reassemble on the surface between tip approaches, suggesting an exchange rate at least 50 times faster than measured in our ATR-IR experiments. At 112 Hz, the barrier height in similar but the thickness of the surfactant layer is much smaller than at lower frequencies, suggesting that the full surfactant film is not able to recover at 112 Hz. The small increase in height between 1 and 14 Hz shows that there is also an adsorption relaxation process in this frequency range.

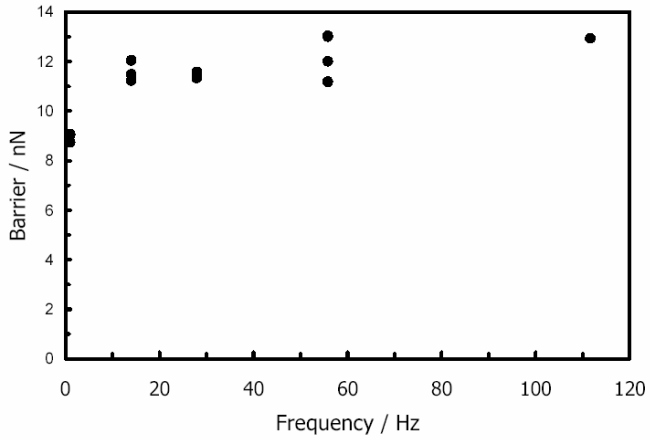

Figure 30. AFM Barrier force as a function of force curve frequency.

5.7 MODELING OF MONOMER EXCHANGE KINETICS

Our experiments that facilitate solution exchange with bubbles show that surfactant exchange is transport limited in the absence of bubbles: faster exchange is observed when the bubble is used to decrease the thickness of the stagnant layer near the surface. Despite this limitation, the observed rates of exchange of deuterated for protonated surfactant are quite fast, and it is interesting to compare the observed rate to the known rate in bulk solution. The desorption rate for a single C_{14}TABr monomer in a bulk micelle is 10^4 s^{-1}. This value was determined by Gharibi et al.[17] based on monomer concentration corrections to the work of Kato et al.[73] Because our results are transport limited, there is little point in making a detailed model of the desorption, but the data do establish a lower bound to the rate.

It is reasonable to assume that only the monomers on the solution side of the micelle can leave; the remainder are prevented or at least hindered from departing by the solid surface. However, exchange between positions in the micelle is very rapid, so that monomers on the solid side can translate around the micelle and then exchange with solution monomers. Furthermore, it is assumed that the rate of exchange is determined by the desorption rather than the adsorption (in keeping with an activated desorption as described by Aniansson et al.)[15], and that the rate constant for protonated monomer desorption is simply proportional to the number of monomers remaining in the micelle (i.e. the activation for desorption is independent of whether the neighbors are protonated or deuterated). A simplified kinetic scheme follows, where there are N consecutive steps in which H exchanges for D.

$$H_{N-x}D_x \rightleftharpoons H_{N\text{-}x\text{-}1}D_x + H \qquad k = \tfrac{1}{2}k'(N-x) \tag{27}$$

Where H represents C_{14}TABr, D represents C_{14}TABr-d_{38}, and k', the rate of desorption for an individual monomer in the micelle. (In Aniansson et al. nomenclature, k' = k/N). The factor of ½ is simply a rough guess as to the fraction of monomers that can leave from a micelle, half of the micelles face the solid and do not interact with the solution. Values of N for C_{14}TABr at the silica-water interface were measured by Ström et al. They are 53, 72, 115, and 143 for concentrations of 1, 2, 3, and 3.1 mM respectively.[31] The 100 or so simultaneous rate equations for aggregates of different composition were solved using Matlab®, and the overall desorption of H was fitted to our measured desorption. In fact, the overall rate is relatively insensitive to the aggregation number in the range N = 70-200. The fitted value of k' was 1 s^{-1}. Thus, the lower bound for the rate of desorption of an individual monomer is 1 s^{-1}, and so the monomer desorption from these adsorbed micelles is no more than 10^4 times slower than from bulk micelles.

Chapter 6 CONCLUSIONS

The research shows that ATR-FTIR is a viable method for quantitation of surface excess and observing surfactant kinetics. One advantage that ATR-FTIR has over ellipsometry, reflectometry, and neutron scattering is the ability to observe the adsorbate spectrum. This capability was used to show that hydrogenated surfactant adsorbs to a greater extent than deuterated surfactant from 1:1 mixtures. In the kinetic experiments it was possible to simultaneously resolve the spectra of the deuterated surfactant, protonated surfactant and D_2O. The data show that the quantity of D_2O in the evanescent zone remained constant during exchange of a surfactant for an isotopically labeled homologue.

It has been shown that the rate of exchange of $C_{14}TABr$ between aqueous solution and the aqueous–silica interface is very rapid: even under conditions where delivery of the new adsorbate to the interface is transport limited, complete exchange in our apparatus occurs within 10 seconds. This corresponds to a fitted rate constant for desorption of $> 1\ s^{-1}$. Thus, the rate of monomer desorption from the surface is no more than 10^4 times slower than the rate of desorption from a bulk micelle. AFM experiments on a faster time scale suggest that surfactant adsorption may even be an additional 500 times faster than measured by ATR-FTIR. An improved method for changing the surface state is required to further reduce the uncertainty in the exchange rates, but at this stage there is no evidence showing that the rate constant for exchange at the interface is smaller than the rate at the surface of a bulk micelle.

Adsorption of surfactant from solution (exchange with solvent and or simple cations) is also a fast process, which in dilute surfactant solutions can be accelerated by pretreating the surface with salt. This suggests that desorption of protons from the silica surface is a rate limiting step in adsorption of the cationic surfactant from a surfactant-only solution. Desorption of surfactant into pure D_2O is also a rapid process, but sufficiently slow compared to the transport rate, that we are able to resolve some structure in the desorption–time profile. Above the cmc, the first $\frac{2}{3}$ of the surfactant desorbs very quickly, and the remainder desorbs slowly. This slow-desorbing fraction is slightly greater in amount than the first plateau in the adsorption isotherm. Exchange of surfactant with salt solution show that this slow-desorbing fraction is held by electrostatic interactions. The results support the conclusion that desorption of ionic surfactant from a charged surface occurs in two stages: rapid loss of surfactant that is held by hydrophobic interactions, and slower loss of surfactant that is held by electrostatic interactions with the surface.

The kinetics of adsorption, desorption, and exchange at 6.3°C (1°C above the freezing point of the solvent and 8°C below the Krafft temperature) is almost the same as at 25.0°C. This is consistent with transport limited processes. There is no indication of a slowing of exchange associated with surface

freezing. However, the density of adsorption is greater, and there is a shift of the IR peak maximum to lower frequency at 6.3 ^{o}C, which shows that the surfactant finds itself in a slightly different state on the surface at the lower temperature.

Chapter 7 FUTURE RESEARCH

7.1 INTRODUCTION

In the present work it has been shown that FTIR coupled with an ATR flow cell is a powerful tool for studying surfactant adsorption, exchange, and desorption at the solid-solution interface. The chief advantages of ATR-FTIR are that it enables one to monitor the adsorption of more than one species simultaneously, *in situ*, with a resolution of about 0.1–2 seconds. Most techniques which measure surface excess are either slower and/or cannot simultaneously and separately measure the adsorption of several species (for example neutron reflection, ellipsometry, reflectometry, solution depletion). FTIR can also provide information about the orientation of the molecules through polarization studies,[8,9,57,62 74] and about intermolecular bonding, though the examination of frequency shifts.[28] A number of research topics well matched to this analytical method are presented below.

7.2 DEVELOPMENT OF THE COLLOIDAL FORCE MICROSCOPE

Total Internal Reflection Microscopy (TIRM) is a technique used to measure colloidal forces between a spherical particle and a transparent plate in solution. A laser is used to generate an evanescent wave at the plate-solution interface. The particle will scatter the evanescent wave, and the scattering intensity is related to the plate-particle separation. This method can be used to quantitate the particle-plate separation instantaneously with a resolution of 1 nm. In a typical TIRM experiment, the freely floating particle will sample a distribution of distances from the interface due to Brownian motion. Attaching the spherical particle to the tip of an Atomic Force Microscope (AFM) cantilever facilitates control of the particle-plate distance and quantitation of the force exerted as the particle is forced into contact with the surface. Quantitation of the particle-plate separation is accomplished using TIRM technology, and ATR spectroscopy at the plate-solution interface will be used to determine adsorbate surface excess *in situ*. Integration of the various technologies into the CFM is shown in Figure 31.

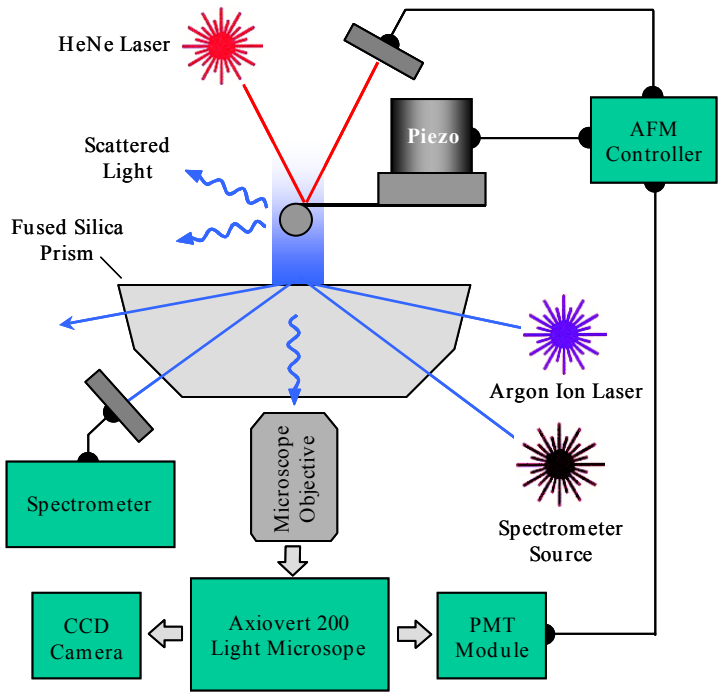

Figure 31. Schematic of the Colloidal Force Microscope (CFM). The CFM is a hybrid of the atomic force microscope and the total internal reflection microscope. It will be possible to obtain particle-plate separation data, force curve data, and determine surface excess simultaneously. Light scattered from the evanescent wave is used to determine particle-plate separation. Force curve data is obtained in the usual manner using a tip-scanning AFM, and surface excess can be determined via fluorescence or ATR spectroscopy.

7.3 Non-Surface Active Infrared Chromophores as a Means of Quantitating Mass Transfer in the Flow Cell

Most researchers have not specified the characteristics of the flow cells used, (such as volume, dead volumes, flow rate, and flow patterns). Absorption research done in other labs may be a function of the equipment used, and not the analyte and substrate. It is evident that our system is transport limited, because were able to reduce transport effects by using the "bubble" method. Quantitation of the transport rate by using non surface active IR active molecules would allow us to distinguish between the transport rate unique to our flow cell and adsorption kinetics of species with where transport is not the limiting factor.

7.3 Mechanical Improvements to the System

Our flow cell is designed to have low volume and no dead volume. In addition, the use of a "bubble" allows us to obtain better kinetic results. I am interested to see what other mechanical improvements can be made to minimize boundary layer effects, thus maximizing the kinetic resolution. Currently, the spectrometer and flow cell are a well-matched kinetic system. The kinetic resolution of the system could be improved by a factor of 10 by increasing the rate at which an analyte is delivered to

the solid-solution interface, and the purchase of faster data acquisition software, such as Omnic Series.

7.4 INVESTIGATE C_{16}TABr KINETICS

A large percentage of kinetic adsorption studies of ionic surfactants have chosen to use C_{16}TABr surfactants on silica as the model because the longer chain surfactants exhibit slower kinetics.[30]

There are inconsistencies among in the literature for C_{16}TABr kinetics on silica, and I would like to conduct my own independent investigation. Velegol and Eskilsson report conflicting results about the initial kinetic adsorption rates for C_{16}TABr as a function of concentration. Eskilsson claims that adsorption is concentration dependent below, and constant above the cmc.[39] Velegol et al. claim the adsorption rate is concentration dependent below and above the cmc, with a jump discontinuity at the cmc. The jump in adsorption rate at the cmc is attributed to direct adsorption of micelles at the silica interface. Velegol et al. used reflectometry and an oxidized silica wafer to do their studies.[37] Repeating their study using ATR-FTIR and an analysis of the asymmetric stretching frequency will give some indication of the adsorbate state, whether they are micelles or monomers.

These experiments would also illustrate that kinetic rates observed by Biswas, Li, and others[42-45] are in fact a function of the experimental design and not the surfactant or substrate.

A fair number of surfactant kinetic and thermodynamic papers include adsorption isotherms of the "purified" surfactant as a guide to its behavior. A surprising number of these contain maxima at the cmc, which demonstrates co-adsorption, where the co-adsorbate is an impurity.[31,37,39,40,48,75,76] Any impurity in the system will dramatically influence the kinetic and thermodynamic behavior. The ability to resolve the adsorbate spectrum allows us to detect some impurities that have gone unnoticed in other systems. Neivandt et al. report that C_{16}TABr will not desorb entirely, even after 20 hours of rinsing,[49] where others report complete desorption in a mater of minutes. Such behavior leads one to suspect that data by Neivandt et al. may be contaminated by compounds which bind irreversibly.[39]

7.5 POLARIZATION MODULATION-ATR-FTIR OF THE DESORPTION PROCESS

Neivandt et al. used a dual-beam FTIR bench and two polarizers mounted on a sample shuttle to acquire dichroic ratio information on C_{16}TABr adsorption and desorption as a function of time.[49,77] Singh et al. conducted a related study on surfactant orientation as a function of surface excess.[6,7] This was an equilibrium study where they stepped the surfactant concentration from zero to the cmc. Dichroic ratios of the surface aggregates were measured after an equilibration period at each step.

The stepped desorption may not yield the same result as a one-step concentration jump with dichroic ratio data acquisition on a fast time scale. Neivandt et al. used their dual beam FTIR bench and a pair of wire-grid polarizers in a sample shuttle to collect dichroic ratio information on a "short" time scale. Neivandt comments that polarization modulation would be the optimal means of studying real time dichroic ratios.[78] Polarization Modulation techniques could easily be used in conjunction with an ATR apparatus to collect dichroic ratio information on a fast time scale. Currently there are no publications where polarization modulation (PM) and ATR-FTIR are used in conjunction. Such a project would be of interest as a new analytical method, and a valuable tool for documenting dichroic ratio changes for kinetic processes, *in situ*.

7.6 CO-ADSORPTION EXPERIMENTS

The ability to resolve infrared spectra of most adsorbates allows us to conduct detailed kinetic and thermodynamic coadsorption studies.[47,70,75,77] A pure surfactant is very rarely used in industrial applications. Some examples of mixed systems include paint, cosmetics, pharmaceuticals, food, personal hygiene products, adhesives, etc.

It would be interesting to compare the kinetics and thermodynamics of pure surfactant systems to mixed systems with intent to deduce the relationship between changes observed in the mixed system and the chemical and physical properties of the coadsorbate/counter ion.[14,27]

7.6.1 Aromatic Coadsorbates

Aromatic molecules are used in fluorescence quenching experiments as probes.[16,31] Benzene could be beneficial in elucidating surface aggregate behavior at concentrations far below the cmc. The benzene spectra in the evanescent zone would serve to signal the formation of hydrophobic regions large enough to stabilize the presence of a moderate sized molecule.[75] Partitioning of benzene between the bulk and the surface aggregates could be observed using ATR-FTIR. Other aromatic hydrocarbons of interest are phenol, benzoic acid, naphthalene or anthracene.

7.6.2 Aliphatic Coadsorbates

Small aliphatic molecules could be used to identify smaller hydrophobic region than the aromatic probes, and possibly provide information about the onset of aggregation at low concentrations, which has been difficult to obtain by AFM. One of the drawbacks of using these small molecules as hydrophobic pocket probes, is they may perturb the adsorption process, thus distorting our perception of the aggregation process. Comparisons between coadsorption studies and adsorption of pure surfactant would be useful to determine the degree that these molecules perturb the system.

7.6.3 Quantitative Deconvolution of Coadsorption Spectra

Use of multivariate analysis would allow us to quantitatively deconvolve composite spectra into its individual spectral components,[79-82] provided one can obtain a pure spectrum of the adsorbates in a

similar environment. This method is also useful in elucidating intermolecular interaction between the adsorbate and co-adsorbate. Spectral changes resulting from component interactions upon co-adsorption will show up in the residuals.

7.7 INFRARED ACTIVE COUNTERION EXPERIMENTS

Research done by Subramanian[83] show that a 10 mM solution of C_{16}TAAc and 100 mM Li_2CO_3 forms hexagonally packed spherical micelles on silica. This same paper explores the influence of divalent counter ions on C_{16}TABr aggregate structure at the silica-solution interface. The counterions used include sulfate, sulfite, thiosulfate, carbonate, and thiocarbonate; all are infrared active divalent anions. The counterion concentration and degree of binding to the interfacial aggregates could be determined. Counterion binding could be compared to structural transitions observed by AFM. Biggs has demonstrated the relationship between counterion binding and surface excess.[37] Infrared active counterions could be used to observe charge regulation at the silica interface and observe exchange of ions for surfactant. In the present work, only the surfactant molecules are observed.

7.8 EXCHANGE KINETICS OF A SURFACTANT BILAYER

Exchange experiments have the potential of providing aggregation details at the solid-liquid interface. Phospholipid molecules form vesicles and bilayers in solution. Monomers tend to translate laterally but the "flip-flop" rate or ability to move from one surface to the other side is relatively low. A surfactant bilayer adsorbed at an interface would behave in a similar fashion. By rapidly exchanging the bulk surfactant with an isotopically labeled one, one can observe the exchange of the surface aggregate molecules with the new bulk solution. All molecules in spherical or cylindrical micelles have access to the bulk solution by translation around the geometric exterior. Monomers incorporated into the underside of a surface adsorbed bilayer would only have access to the solution by diving through the bilayer.

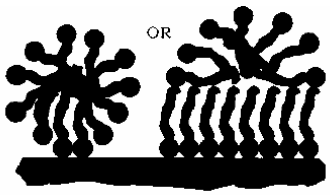

Figure 32. Schematic representation of surfactant adsorption at the silica-solution interface as inferred from AFM images.

The same procedure used to observe exchange kinetics of C_{14}TABr could be used to determine the kinetic exchange of the bulk solution with the bilayer underside. This system could be used to elucidate some information about the underlying aggregate structure.

If the bilayer kinetic exchange experiment performs as hypothesized, it would infer that the "hemisphere on monolayer" structure is not the underlying C_{14}TABr structure as suggested in some earlier work.[4-7]

References

1. McBain, J. C.; Salmon, C. S., Colloidal Electrolytes. Soap Solutions and Their Constitution. *J. Phys. Chem.* **1920,** *42*, 426-460.

2. Hartley, G. S.; Collie, B.; Samis, C. S., *Trans. Faraday Soc.* **1936,** *32*, 795.

3. Mijnlieff, P. F.; Ditmarsch, R., *Nature* **1965,** *208*, 889.

4. Liu, J.-F.; Ducker, W. A., Surface-Induced Phase Behavior of Alkyltrimethylammonium Bromide Surfactants Adsorbed to Mica, Silica, and Graphite. *J. Phys. Chem. B* **1999,** *103*, 8558-8567.

5. Subramanian, V.; Ducker, W. A., Proximal Adsorption of Cationic Surfactant on Lilica at Equilibrium. *J. Phys. Chem. B* **2001,** *105*, 1389-1402.

6. Adler, J. J.; Singh, P. K.; Patist, A.; Rabinovich, Y. I.; Shah, D. O.; Moudgil, B. M., Correlation of Particulate Dispersion Stability with the Strength of Self-Assembled Surfactant Films. *Langmuir* **2000,** *16*, 7255-7262.

7. Singh, P. K.; Adler, J. J.; Rabinovich, Y. I.; Moudgil, B. M., Investigation of Self-assembled Surfactant Structure at the Solid-Liquid Interface Using FTIR/ATR. *Langmuir* **2001,** *17*, 468-473.

8. Citra, M. J.; Axelsen, P. H., Determination of Molecular Order in Supported Lipid Membranes by Internal Reflection Fourier Transform Infrared Spectroscopy. *Biophys. J.* **1996,** *71*, 1796-1805.

9. Picard, F.; Buffeteau, T.; Desbat, B.; Auger, M.; Pézolet, M., Quantitative Orientation Measurements in Thin Lipid Films by Attenuated Total Reflection Infrared Spectroscopy. *Biophys. J.* **1999,** *76*, 539-551.

10. Evans, D. F.; Wennerström, H., *The Colloidal Domain*. 1st ed.; VCH Publishers, Inc.: New York, 1994; p 515.

11. Huibers, P. D. T.; Oh, S. G.; Shah, D. O., Pressure Jump Studies on Micellar Relaxation Time and its Effect on Various Technological Processes. In *Surfactants in Solution*, ed.; Chattopadhyay, A. K.; Mittal, K. L., Marcel dekker, Inc.: New York, 1996; Vol. 64, pp 105-122.

12. Gruen, D. W. R., A Model for the Chains in Amphiphilic Aggregates. 1. Comparison with a Molecular Dynamics Simulation of a Bilayer. *J. Phys. Chem. B* **1985,** *89*, 146-153.

13. Gruen, D. W. R., A Model for the Chains in Amphiphilic Aggregates. 2. Thermodynamic and Experimental Comparisons for Aggregates of Different Shape and Size. *J. Phys. Chem. B* **1985,** *89*, 153-163.

14. Patist, A.; Kanicky, J. R.; Shukla, P. K.; Shah, D. O., Importance of Micellar Kinetics in Relation to Technological Processes. *J. Colloid Interface Sci.* **2002,** *245*, 1-15.

15. Aniansson, E. A. G.; Wall, S. N.; Almgren, M.; Hoffmann, H.; Kielmann, I.; Ulbricht, W.; Zana, R.; Lang, J.; Tondre, C., Theory of the Kinetics of Micellar Equilibria and Quantitative Interpretation of Chemical Relaxation Studies of Micellar Solutions of Ionic Surfactants. *J. Phys. Chem. B* **1976,** *80*, (9), 905-922.

16. Hansson, P.; Jönsson, B.; Ström, C.; Söderman, O., Determination of Micellar Aggregation Numbers in dilute Surfactant Systems with the Fluorescence Quenching Method. *J. Phys. Chem. B* **2000,** *104*, 3496-3506.

17. Gharibi, H.; Takisawa, N.; Brown, P.; Thomason, M. A.; Painter, D. M.; Bloor, D. M.; Hall, D. G.; Wyn-Jones, E., Analysis of the Fast Relaxation Times for Micelle Kinetics taking into account new EMF Data. *J. Chem. Soc., Faraday Trans.* **1991,** *87*, 707-710.

18. Kahlweit, M., Kinetics of Formation of Association Colloids. *J. Colloid Interface Sci.* **1982,** *90*, 92-99.

19. Lessner, E.; Teubner, M.; Kahlweit, M., Relaxation Experiments in Aqueous Solutions of Ionic Micelles. 2. Experiments on the System H_2O-NaDS-$NaClO_4$ and Their Theoretical Interpretation. *J. Phys. Chem.* **1981,** *85*, 3167-3175.

20. Ulbricht, W.; Zana, R., Alkanediyl-alpha,omega-bis(dimethylalkylammonium bromide) surfactants Part 8. Pressure-jump study of the kinetics of micellar equilibria in aqueous solutions of alkanediyl-alpha,omega-bis(dimethyldodecylammonium bromide) surfactants. *Colloids Surf., A* **2001,** *183-185*, 487-494.

21. Frindi, M.; Michels, B.; Zana, R., Ultrasonlc Absorption Studies of Surfactant Exchange between Micelles and Bulk Phase In Aqueous Micellar Solutions of Nonionic Surfactants with Short Alkyl Chains. 1. 1,2-HexanedIol and 1,2,3-0ctanetriol. *J. Phys. Chem. B* **1991,** *95*, 4832-4837.

22. Frindi, M.; Michels, B.; Zana, R., Ultrasonic Absorption Studles of Surfactant Exchange between Mlcelles and Bulk Phase in Aqueous Micellar Solutions of Nonionic Surfactants with a Short Alkyl Chain. 2. C6E3, C6E5, C8E4, and C8E8. *J. Phys. Chem. B* **1992,** *96*, 6095-6102.

23. Frindi, M.; Michels, B.; Zana, R., Ultrasonic Absorption Studies of Surfactant Exchange between Micelles and Bulk Phase in Aqueous Micellar Solutlons of Nonionic Surfactants with a Short Alkyl Chain. 3. Surfactants with a Sugar Head Group. *J. Phys. Chem. B* **1992,** *96*, 8137-8141.

24. Oh, S. G.; Shah, D. O., *Journal of the American Oil Chemist's Society* **1993,** *70*, 673.

25. Oh, S. G.; Jobalia, M.; Shah, D. O., The Effect of Micellar Lifetime on the Droplet Size in Emulsions. *J. Colloid Interface Sci.* **1993,** *155*, 511-514.

26. Cross, W. M.; Kellar, J. J.; Miller, J. D., Fourier Transform Near-Infrared Examination of the Coagel-to-Micelle Transition for Sodium Laurate. *Appl. Spectrosc.* **1992**, *46*, (4), 701-704.

27. Ninness, B. J.; Bousfield, D. W.; Tripp, C. P., The importance of adsorbed cationic surfactant structure in dictating the subsequent interaction of anionic surfactants and polyelectrolytes with pigment surfaces. *Colloids Surf., A* **2002,** *203*, 21-36.

28. Sperline, R. P., Infrared Spectroscopic Study of the Crystalline Phases of Sodium Dodecyl Sulfate. *Langmuir* **1997,** *13*, 3715-3726.

29. Atkin, R.; Craig, V. S. J.; Biggs, S., Adsorption Kinetics and Structural Arrangements of Cetylpyridinium Bromide at the Silica-Aqueous Interface. *Langmuir* **2001,** *17*, 6155-6163.

30. Tiberg, F.; Jönsson, B.; Lindaman, B., Ellipsometry Studies of the Self-Assembly of Nonionic Surfactants at the Silica-Water Interface: Kinetic Aspects. *Langmuir* **1994,** *10*, 3714-3722.

31. Ström, C.; Hansson, P.; Jönsson, B.; Söderman, O., Size of Cationic Surfactant Micelles at the Silica-Water Interface: A Fluorescent Probe Study. *Langmuir* **2000,** *16*, 2469-2474.

32. Manne, S.; Gaub, H. E., Molecular Organization of Surfactants at Solid-Liquid Interfaces. *Science* **1995,** *270*, 1480-1482.

33. Manne, S., Visualizing self-assembly: Force microscopy of ionic surfactant aggregates at solid-liquid interfaces. *Prog. Colloid Polym. Sci.* **1997,** *103*, 226-233.

34. Rennie, A. R., Structure of Cationic Surfactant Layer at the Silica-Water Interface. *Langmuir* **1990,** *6*, 1031-1034.

35. McDermott, D. C.; McCarney, J.; Thomas, R. K., Study of an adsorbed layer of Hexadecyltrimethylammonium Bromide Using the Technique of Neutron Reflection. *J. Colloid Interface Sci.* **1994,** *162*, 304-310.

36. Alargova, R. G.; Kochijasky, I. I.; Sierra, M. L.; Zana, R., Micelle Aggregation Numbers of Surfactants in Aqueous Solutions: A Comparison between The Results from Steady-State and Time-Resolved Fluorescence Quenching. *Langmuir* **1998,** *14*, 5412-5418.

37. Velegol, S. B.; Fleming, B. D.; Biggs, S.; Wanless, E. J.; Tilton, R. D., Counterion Effects on Hexadecyltrimethylammonium Surfactant Adsorption and Self-Assembly on Silica. *Langmuir* **2000,** *16*, 2548-2556.

38. Couzis, A.; Gulari, E., Adsorption of Sodium Laurate from Its Aqueous Solution onto an Alumina Surface. A Dynamic Study of the Surface-Surfactant Interaction Using Attenuated Total Reflection Fourier Transform Infrared Spectroscopy. *Langmuir* **1993,** *9*, 3414-3421.

39. Eskilsson, K.; Yaminsky, V. V., Deposition of Monolayers by Retraction from Solution: Ellipsometric Study of Cetyltrimethylammonium Bromide Adsorption at Silica-Air and Silica-Water Interfaces. *Langmuir* **1998,** *14*, 2444-2450.

40. Pagac, E. S.; Prieve, D. C.; Tilton, R. D., Kinetics and Mechanism of Cationic Surfactant Adsorption and Coadsorption with Cationic Polyelectrolytes at the Silica-Water Interface. *Langmuir* **1998,** *14*, 2333-2342.

41. MacLeod, C. A.; Radke, C. J., Charge Effects in the Transient Adsorption of Ionic Surfactants at Fluid Interfaces. *Langmuir* **1994,** *10*, 3555-3566.

42. Biswas, S. C.; Chattoraj, D. K., Kinetics of Adsorptin of Cationic Surfactants at Silica-Water Interface. *J. Colloid Interface Sci.* **1998,** *205*, 12 - 20.

43. Li, Z., Sorption Kinetics of Hexadecyltrimethylammonium on Natural Clinoptilolite. *Langmuir* **1999,** *15*, 6438-6445.

44. Partyka, S.; Zaini, S.; Lindheimer, M.; Brun, B., The Adsorption of Non-Ionic Surfactants on a Silica Gel. *Colloids Surf.* **1984,** *12*, 255-270.

45. Ghosh, L.; Das, K. P.; Chattoraj, D. K., Kinetics of Adsorption of Ionic Surfactants at Alumina-Water Interface. *J. Indian Chem. Soc.* **1986,** *63*, 144-148.

46. Frantz, P.; Leonhardt, D. C.; Granick, S., Enthalpic Effects in Competitive Polymer Adsorption: Adsorption Isotope Effect and Chain End Effect. *Macromolecules* **1991,** *24*, 1868-1875.

47. Frantz, P.; Granick, S., Surface Preparation of Silicon for Polymer Adsorption Studies. *Langmuir* **1992,** *8*, 1176-1182.

48. Atkin, R.; Craig, V. S. J.; Biggs, S., Adsorption Kinetics and Structural Arrangements of Cationic Surfactants on Silica Surfaces. *Langmuir* **2000,** *16*, 9374-9380.

49. Neivandt, D. J.; Gee, M. L.; Hair, M. L.; Tripp, C. P., Polarized Infrared Attenuated Total Reflection for the in Situ Determination of the Orientation of Surfactant Adsorbed at the Solid/Solution Interface. *J. Phys. Chem. B* **1998,** *102*, (26), 5107-5114.

50. Neivandt, D. J.; Gee, M. L.; Tripp, C. P.; Hair, M. L., Coadsorption of Poly(styrenesulfonate) and Cetyltrimethylammonium Bromide on Silica Investigated by Attenuated Total Reflection Techniques. *Langmuir* **1997,** *13*, 2519-2526.

51. Harrick, N. J., Electric Field Strengths at Totally Reflecting Interfaces. *J. Opt. Soc. Am.* **1965,** *55*, (7), 851-857.

52. Harrick, N. J., *Internal Reflection Spectroscopy*.; Interscience Publishers: New York, 1967

53. Hansen, W. N., Electric Fields Produced by the Propagation of Plane Coherent Electromagnetic Radiation in a Stratified Medium. *J. Opt. Soc. Am.* **1968,** *58*, (3), 380-390.

54. Hansen, W. N., Internal Reflection Spectroscopy in Electrochemistry. In *Advances in Electrochemistry and Electrochemical Engineering*.; Delahay, P.; Tobias, C. W., John Wiley & Sons: New York, 1973; Vol. 9, pp 1 - 60.

55. Hansen, W. N.; Kuwana, T.; Osteryoung, R. A., Observation of Electrode-Solution Interface by Means of Internal Reflection Spectrometry. *Anal. Chem.* **1966,** *38*, (13), 1810 - 1821.

56. Koppaka, V.; Axelsen, P. H., Evanescent Electric Field Amplitudes in Thin Lipid Films for Internal Reflection Infrared Spectroscopy. *Langmuir* **2001,** *17*, 6309-6316.

57. Sperline, R. P.; Song, Y.; Freiser, H., Fourier Transform Infrared Attenuated Total Reflection Spectroscopy Linear Dichroism Study of Sodium Dodecyl Sulfate Adsorption at the Al_2O_3/Water Interface using Al_2O_3-Coated Optics. *Langmuir* **1992,** *9*, 2183.

58. Jeon, J. S.; Sperline, R. P.; Raghavan, S., Quantitative Analysis of Adsorbed Serum Albumin on Segmented Polyurethane Using FT-IR/ATR Spectroscopy. *Appl. Spectrosc.* **1992,** *46*, (11), 1644-1648.

59. Sperline, R. P.; Freiser, H., Adsorption at the Liquid-Liquid Interface Analyzed by in Situ Infrared Attenuated Total Reflection Spectroscopy. *Langmuir* **1990,** *6*, 344 - 347.

60. Thompkins, H. G., The Physical Basis for Analysis of the Depth of Absorbing Species Using Internal Reflection Spectroscopy. *Appl. Spectrosc.* **1974,** *28*, 335 - 341.

61. Reichert, W. M., Evanescent Detection of Adsorbed Films: Assessment of Optical Considerations for absrbance and Fluorescence Spectroscopy at The Crystal/Solution and Polymer/Solution Interfaces. *CRC Rev. Biocomp.* **1989,** *5*, (2), 173-205.

62. Sperline, R. P.; Song, Y.; Freiser, H., Fourier Transform Infrared Attenuated Total Reflection Linear Dichroism Study of Sodium Dodecylbenzenesulfonate Adsorption at the Al_2O_3/Water Interface Using Al_2O_3-coated Optics. *Langmuir* **1994,** *10*, 37-44.

63. Sperline, R. P., Analytical accuracy in unpolarized ATR spectroscopy: effects of the spectrometer polarization ratio. *Appl. Spectrosc.* **1991,** *45*, (4), 677-81.

64. Bertie, J. E.; Ahmed, M. K.; Eysel, H. H., Infrared Intensities of Liquids. 5. Optical and Dielectric Constants, Integrated Intensities, and Dipole Moment Derivatives of H_2O and D_2O at 22 Celsius. *J. Phys. Chem. B* **1989,** *93*, 2210-2218.

65. Brunner, H.; Vallant, T.; Mayer, U.; Hoffmann, H., Stepwise Growth of Ultrathin SiOx Films on Si(100) Surfaces through Sequential Adsorption/Oxidation Cycles of Alkylsiloxane Monolayers. *Langmuir* **1996,** *12*, 4614-4617.

66. Sperline, R. P.; Song, Y.; Freiser, H., Temperature Dependent Structure of Adsorbed Sodium Dodecyl Sulfate at the Al_2O_3/Water Interface. *Langmuir* **1997,** *13*, 3727-3732.

67. Kawai, T.; Umemura, J.; Takenaka, T., Polarized Fourier Transform Infrared Spectra and Molecular Orientation of a Water-Dioctadecyldimethylammonium Chloride System in the Coagel and Gel Phases. *Langmuir* **1986,** *2*, 739-743.

68. Griffiths, P. R.; de Haseth, J. A., *Fourier Transform Infrared Spectroscopy*.; Wiley: New York, 1986

69. Sperline, R. P.; Muralidharan, S.; Freiser, H., New quantitative technique for attenuated total reflection (ATR) spectrophotometry; calibration of the CIRCLE ATR device in the infrared. *Appl. Spectrosc.* **1986,** *40*, (7), 1019-22.

70. Johnson, H. E.; Granick, S., Exchange Kinetics between the Adsorbed State and Free Solution: Poly(methyl methacrylate) in Carbon Tetrachloride. *Macromolecules* **1990,** *23*, 3367-3374.

71. Goloub, T. P.; Koopal, L. K.; Bijsterbosch, B. H.; Sidorova, M. P., Adsorption of Cationic Surfactants on Silica. Surface Charge Effects. *Langmuir* **1996,** *12*, 3188-3194.

72. Walz, J., Private communication.

73. Kato, S.; Nomura, H.; Honda, H.; Zielinski, R.; Ikeda, S., Ultrasonic Relaxation Study of the Exchange Process of Surfactant Monomer with Micelle in Aqueous Solutions of Alkyltrimethylammonium Bromides. *J. Phys. Chem.* **1988,** *92*, 2305-2310.

74. Vallant, T.; Kattner, J.; Brunner, H.; Mayer, U.; Hoffmann, H., Investigation of the Formation and Structure of Self-assembled Alkylsiloxane Monolayers on Silicon Using In Situ Attenuated Total Reflection Infrared Spectroscopy. *Langmuir* **1999,** *15*, 5339-5346.

75. Favoriti, P.; Monticone, V.; Treiner, C., Coadsorption of naphthalene derivatives and cetyltrimethylammonium bromide on alumina/water, titanium dioxide/water, and silica/water interfaces. *J. Colloid Interface Sci.* **1996,** *179*, (1), 173-180.

76. Wängnerud, P.; Jönsson, B., Adsorption of Ionic Amphiphiles as Bilayers on Charged Surfaces. *Langmuir* **1994,** *10*, 3268-3278.

77. Soga, I.; Granick, S., Infrared Dichroism and Surface Conformational Dynamics of Adsorbed Poly(dimethylsiloxane). *Macromolecules* **1998,** *31*, 5450-5455.

78. Golden, W. G.; Saperstein, D. D.; Severson, M. W.; Overend, J., Infrared Reflection-Absorption Spectroscopy of Surface Species: A Comparison of Fourier Transform and Despersion Methods. *J. Phys. Chem.* **1984,** *88*, 574-580.

79. Rivera, D.; Harris, J. M., In Situ ATR-FT-IR Kinetic Studies of Molecular Transport and Surface Binding in Thin Sol-Gel Films: Reactions of Chlorosilane Reagents in Porous Silica Materials. *Anal. Chem.* **2001,** *73*, 411-423.

80. Haaland, D. M.; Han, L.; Niemczyk, T. M., Use of CLS to Understand PLS IR Calibration for Trace Detection of Organic Molecules in Water. *Appl. Spectrosc.* **1999,** *53*, (4), 390-395.

81. Schulz, H.; Schrader, B.; Quilitzsch, R.; Steuer, B., Quantitative Analysis of Various Citrus Oils by ATR/FT-IR and NIR-FT Raman Spectroscopy. *Appl. Spectrosc.* **2002,** *56*, (1), 117-124.

82. Heise, H. M.; Marbach, R.; Janatsch, G.; Kruse-Jarres, J. D., Multivariate Determination of Glucose in Whole Blood by Attenuated Total Reflection Infrared Spectroscopy. *Anal. Chem.* **1989,** *61*, 2009-2015.

83. Subramanian, V.; Ducker, W. A., Counterion Effects on Adsorbed Micellar Shape: Experimental Study of the Role of Polarizability and Charge. *Langmuir* **2000,** *16*, 4447-4454.

Appendix A MAPLE 7.0 WORKSHEETS

A.1 MEAN SQUARE ELECTRIC FIELD AT 2159 RECIPROCAL CENTIMETERS

References:

1. Hansen, W. N. *Jnl of the Optical Society of America* 1968, *58*, 380
2. Hansen, W. N. Internal reflection spectroscopy in electrochemistry. *Advances in Electrochemistry and Electrochemical Engineering* 1973, *9*, 1-60
3. Hansen, W. N. *Analytical Chemistry* 1966, *38*, 1810
4. Citra, M. J.; Axelsen, P. H. *Biophysical Journal* 1996, *71*, 1796
5. Picard, F.; Buffeteau, T.; Desbat, B.; Auger, M. Pezolet, M. *Biophysical Journal* 1999, *76*, 539
6. D:\MathCad\Gibbs Surface Excess.mcd


```
> restart:
```

Incident angle

```
> theta:=(49.332/180)*Pi:
```

Wavelength

```
> lamda:=(215900*meter^(-1))^(-1):
> evalf(lamda);
```

$.4631773969\,10^{-5}\ meter$

Medium 1 complex refractive index input

```
> n1:=3.4249:
> k1:=0.000:
> n1_cpx:=Complex(n1,k1);
```

$n1\_cpx := 3.4249 + 0.\ I$

Medium 2 complex refractive index input

```
> n2:=1.399:
> k2:=0.0137:
> n2_cpx:=Complex(n2,k2);
```

$n2\_cpx := 1.399 + .0137\ I$

Second medium thickness

```
> h:=(0E-9)*meter;
```

$h := 0.$

Mean square electric field strength calculated at distance z from the n1|n2 interface

```
> z:=(0E-9)*meter;
```

$z := 0.$

Medium 3 complex refractive index input

```
> n3:=1.399:
> k3:=0.0137:
> n3_cpx:=Complex(n3,k3);
```

$n3\_cpx := 1.399 + .0137\,I$

Define xi for n1, n1|n2, and n2|n3 interface

```
> xi1:=n1_cpx*cos(theta):
> xi2:=sqrt((n2_cpx^2)-(n1^2)*(sin(theta))^2):
> xi3:=sqrt((n3_cpx^2)-(n1^2)*(sin(theta))^2):
```

Beta for second medium

```
> beta:=2*Pi*xi3*(h/lamda):
```

Fresnel Coefficients for the n1|n2 interface

```
> rs12:=(xi1-xi2)/(xi1+xi2):
> rp12:=(n2_cpx^2*xi1-n1_cpx^2*xi2)/(n2_cpx^2*xi1+n1_cpx^2*xi2):
> ts12:=2*xi1/(xi1+xi2):
> tp12:= 2*n2_cpx^2*xi1/(n2_cpx^2*xi1+n1_cpx^2*xi2):
```

Fresnel Coefficients for the n2|n3 interface

```
> rs23:=(xi2-xi3)/(xi2+xi3):
> rp23:=(n3_cpx^2*xi2-n2_cpx^2*xi3)/(n3_cpx^2*xi2+n2_cpx^2*xi3):
> ts23:=2*xi2/(xi2+xi3):
> tp23:= 2*n3_cpx^2*xi2/(n3_cpx^2*xi2+n2_cpx^2*xi3):
```

Combined Fresnel Coefficients for s and p components

```
> ts := ts12*ts23*exp(I*beta)/(1+rs12*rs23*exp(2*I*beta)):
> tp := (n1/n3_cpx)*(tp12*tp23*exp(I*beta))/(1+rp12*rp23*exp(2*I*beta)):
```

Mean square electric field strengths in the x, y, and z directions

```
> Ex:=((abs(tp*xi3/n3_cpx))^2)*exp(-4*Pi*(z-h)*Im(xi3)/lamda):
> Ey:=((abs(ts))^2)*exp(-4*Pi*(z-h)*Im(xi3)/lamda):
> Ez:=((abs(tp*n1*sin(theta)/n3_cpx))^2)*exp(-4*Pi*(z-h)*Im(xi3)/lamda):
> evalf(Ex); evalf(Ey); evalf(Ez);
```

1.638151097

2.030733344

2.307160906

Evaluation of Harrick's Two Medium Approximation

```
> Exo:=(4*(cos(theta))^2*((sin(theta))^2-(n3/n1)^2)/((1-(n3/n1)^2)*((1+(n3/n1)^2)*(sin(theta)^2)-(n3/n1)^2))):
> Eyo:=4*(cos(theta))^2/(1-(n3/n1)^2):
> Ezo:=(4*(cos(theta))^2*((sin(theta))^2)/((1-(n3/n1)^2)*((1+(n3/n1)^2)*(sin(theta)^2)-(n3/n1)^2))):
> evalf(Exo); evalf(Eyo); evalf(Ezo);
```

1.650932897

2.038925901

2.325328201

Penetration Depth value

```
> dd:=lamda/(4*Pi*Im(xi3)):
> evalf(dd);
```

$.1683838193\ 10^{-6}$ *meter*

Evaluation of b_{eff} for unpolarized experiment "unp", isotropic absorber "iso"

```
> PR:=0.5633:
> beff_s:=(dd*Ey*n3)/(n1*cos(theta)):
> beff_p:=(dd*Ex*n3)/(n1*cos(theta))+(dd*Ez*n3)/(n1*cos(theta)):
> beff_unp:=((PR*beff_s)/(PR+1))+(beff_p/(PR+1)):
> evalf(beff_unp);
```

$.3435962706\ 10^{-6}$ *meter*

A.2 MEAN SQUARE ELECTRIC FIELD AT 2910 RECIPROCAL CENTIMETERS

References:

1. Hansen, W. N. *Jnl of the Optical Society of America* 1968, *58*, 380
2. Hansen, W. N. Internal reflection spectroscopy in electrochemistry. *Advances in Electrochemistry and Electrochemical Engineering* 1973, *9*, 1-60
3. Hansen, W. N. *Analytical Chemistry* 1966, *38*, 1810
4. Citra, M. J.; Axelsen, P. H. *Biophysical Journal* 1996, *71*, 1796
5. Picard, F.; Buffeteau, T.; Desbat, B.; Auger, M. Pezolet, M. *Biophysical Journal* 1999, *76*, 539
6. D:\MathCad\Gibbs Surface Excess.mcd


```
> restart:
```

Incident angle

```
> theta:=(49.332/180)*Pi:
```

Wavelength

```
> lamda:=(291000*meter^(-1))^(-1):
> evalf(lamda);
```

$.34364261117\,10^{-5}\ meter$

Medium 1 complex refractive index input

```
> n1:=3.4302:
> k1:=0.0000:
> n1_cpx:=Complex(n1,k1);
```

$n1\_cpx := 3.4302 + 0.\ I$

Medium 2 complex refractive index input

```
> n2:=1.236:
> k2:=0.00222:
> n2_cpx:=Complex(n2,k2);
```

$n2\_cpx := 1.236 + .00222\ I$

Second medium thickness

```
> h:=(0E-9)*meter;
```

$h := 0.$

Mean square electric field strength calculated at distance z from the n1|n2 interface

```
> z:=(0E-9)*meter;
```

$z := 0.$

Medium 3 complex refractive index input

```
> n3:=1.236:
> k3:=0.00222:
> n3_cpx:=Complex(n3,k3);
```

$$n3\_cpx := 1.236 + .00222\,I$$

Define xi for n1, n1|n2, and n2|n3 interface

```
> xi1:=n1_cpx*cos(theta):
> xi2:=sqrt((n2_cpx^2)-(n1^2)*(sin(theta))^2):
> xi3:=sqrt((n3_cpx^2)-(n1^2)*(sin(theta))^2):
```

Beta for second medium

```
> beta:=2*Pi*xi3*(h/lamda):
```

Fresnel Coefficients for the n1|n2 interface

```
> rs12:=(xi1-xi2)/(xi1+xi2):
> rp12:=(n2_cpx^2*xi1-n1_cpx^2*xi2)/(n2_cpx^2*xi1+n1_cpx^2*xi2):
> ts12:=2*xi1/(xi1+xi2):
> tp12:= 2*n2_cpx^2*xi1/(n2_cpx^2*xi1+n1_cpx^2*xi2):
```

Fresnel Coefficients for the n2|n3 interface

```
> rs23:=(xi2-xi3)/(xi2+xi3):
> rp23:=(n3_cpx^2*xi2-n2_cpx^2*xi3)/(n3_cpx^2*xi2+n2_cpx^2*xi3):
> ts23:=2*xi2/(xi2+xi3):
> tp23:= 2*n3_cpx^2*xi2/(n3_cpx^2*xi2+n2_cpx^2*xi3):
```

Combined Fresnel Coefficients for s and p components

```
> ts := ts12*ts23*exp(I*beta)/(1+rs12*rs23*exp(2*I*beta)):
> tp := (n1/n3_cpx)*(tp12*tp23*exp(I*beta))/(1+rp12*rp23*exp(2*I*beta)):
```

Exact mean square electric field strengths in the x, y, and z directions

```
> Ex:=((abs(tp*xi3/n3_cpx))^2)*exp(-4*Pi*(z-h)*Im(xi3)/lamda):
> Ey:=((abs(ts))^2)*exp(-4*Pi*(z-h)*Im(xi3)/lamda):
> Ez:=((abs(tp*n1*sin(theta)/n3_cpx))^2)*exp(-4*Pi*(z-h)*Im(xi3)/lamda):
> evalf(Ex); evalf(Ey); evalf(Ez);
```

1.670137892

1.951163784

2.156899605

Evaluation of Harrick's Two Medium Approximation

```
> Exo:=(4*(cos(theta))^2*((sin(theta))^2-(n3/n1)^2)/((1-(n3/n1)^2)*((1+(n3/n1)^2)*(sin(theta)^2)-(n3/n1)^2))):
> Eyo:=4*(cos(theta))^2/(1-(n3/n1)^2):
> Ezo:=(4*(cos(theta))^2*((sin(theta))^2)/((1-(n3/n1)^2)*((1+(n3/n1)^2)*(sin(theta)^2)-(n3/n1)^2))):
> evalf(Exo); evalf(Eyo); evalf(Ezo);
```

1.671853228

1.952186376

2.159118089

Penetration Depth value

```
> dd:=lamda/(4*Pi*Im(xi3)):
> evalf(dd);
```

$.1194433251\ 10^{-6}\ meter$

Evaluation of b_{eff} for unpolarized experiment "unp", isotropic absorber "iso"

```
> PR:=0.5655:
> beff_s:=(dd*Ey*n3)/(n1*cos(theta)):
> beff_p:=(dd*Ex*n3)/(n1*cos(theta))+(dd*Ez*n3)/(n1*cos(theta)):
> beff_unp:=((PR*beff_s)/(PR+1))+(beff_p/(PR+1)):
> evalf(beff_unp);
```

$.2079988009\ 10^{-6}\ meter$

A.3 GIBBS SURFACE EXCESS FROM INTEGRATED -LOG(R) AT 2159 RECIPROCAL CENTIMETERS

Gibbs Surface Excess from Integrated -log(R) ATR Spectra

Based on Mean Square Electric Fields Calculated from Derivations by Wilford Hansen
with Sperline Polarization Ratio Modification

Filename: Gibbs Surface Excess @ 2159.mws (60 degree incident angle)
Date: 30 October 2002

References:

1. Hansen, W. N. *Jnl of the Optical Society of America* 1968, *58*, 380
2. Hansen, W. N. Internal reflection spectroscopy in electrochemistry. *Advances in Electrochemistry and Electrochemical Engineering* 1973, *9*, 1-60
3. Hansen, W. N. *Analytical Chemistry* 1966, *38*, 1810
4. Citra, M. J.; Axelsen, P. H. *Biophysical Journal* 1996, *71*, 1796
5. Picard, F.; Buffeteau, T.; Desbat, B.; Auger, M. Pezolet, M. *Biophysical Journal* 1999, *76*, 539
6. D:\MathCad\Gibbs Surface Excess.mcd

Experimental Parameter Inputs

> restart:

Number of internal reflections

> N:=22:

Concentration of Bulk Solution

> Conc:=0.005001*mol/(1E-1*meter)^3;

$$Conc := 5.001000000 \frac{mol}{meter^3}$$

Transmission molar extinction coefficient

> epsilon := 1688018.126*(1/meter)*(((0.1*meter)^3)/mol);

$$\varepsilon := 1688.018126 \frac{meter^2}{mol}$$

Incident angle

> theta:=(49.332/180)*Pi:

Wavelength

```
> lamda:=(215900*meter^(-1))^(-1):
> evalf(lamda);
```

$.4631773969\,10^{-5}\ meter$

Medium 1 complex refractive index input

```
> n1:=3.4249:
> k1:=0.0000:
> n1_cpx:=Complex(n1,k1);
```

$n1\_cpx := 3.4249 + 0.\ I$

Medium 2 complex refractive index input

```
> n2:=1.399:
> k2:=0.0137:
> n2_cpx:=Complex(n2,k2);
```

$n2\_cpx := 1.399 + .0137\ I$

Second medium thickness

```
> h:=(0E-9)*meter;
```

$h := 0.$

Mean square electric field strength calculated at distance z from the n1|n2 interface

```
> z:=(0E-9)*meter;
```

$z := 0.$

Medium 3 complex refractive index input

```
> n3:=1.399:
> k3:=0.0137:
> n3_cpx:=Complex(n3,k3);
```

$n3\_cpx := 1.399 + .0137\ I$

Calculation of Mean Square Electric Fields

Define xi for n1, n1|n2, and n2|n3 interface

```
> xi1:=n1_cpx*cos(theta):
> xi2:=sqrt((n2_cpx^2)-(n1^2)*(sin(theta))^2):
> xi3:=sqrt((n3_cpx^2)-(n1^2)*(sin(theta))^2):
```

Beta for second medium

```
> beta:=2*Pi*xi3*(h/lamda):
```

Fresnel Coefficients for the n1|n2 interface

```
> rs12:=(xi1-xi2)/(xi1+xi2):
> rp12:=(n2_cpx^2*xi1-n1_cpx^2*xi2)/(n2_cpx^2*xi1+n1_cpx^2*xi2):
> ts12:=2*xi1/(xi1+xi2):
> tp12:= 2*n2_cpx^2*xi1/(n2_cpx^2*xi1+n1_cpx^2*xi2):
```

Fresnel Coefficients for the n2|n3 interface

```
> rs23:=(xi2-xi3)/(xi2+xi3):
> rp23:=(n3_cpx^2*xi2-n2_cpx^2*xi3)/(n3_cpx^2*xi2+n2_cpx^2*xi3):
> ts23:=2*xi2/(xi2+xi3):
> tp23:= 2*n3_cpx^2*xi2/(n3_cpx^2*xi2+n2_cpx^2*xi3):
```

Combined Fresnel Coefficients for s and p components

```
> ts := ts12*ts23*exp(I*beta)/(1+rs12*rs23*exp(2*I*beta)):
> tp := (n1/n3_cpx)*(tp12*tp23*exp(I*beta))/(1+rp12*rp23*exp(2*I*beta)):
```

Exact mean square electric field strengths in the x, y, and z directions

```
> Ex:=((abs(tp*xi3/n3_cpx))^2)*exp(-4*Pi*(z-h)*Im(xi3)/lamda):
> Ey:=((abs(ts))^2)*exp(-4*Pi*(z-h)*Im(xi3)/lamda):
> Ez:=((abs(tp*n1*sin(theta)/n3_cpx))^2)*exp(-4*Pi*(z-h)*Im(xi3)/lamda):
> evalf(Ex); evalf(Ey); evalf(Ez);
```

```
1.638151097

2.030733344

2.307160906
```

Approximate mean square electric field strengths (Harrick approximation)

```
>          Exo:=(4*(cos(theta))^2*((sin(theta))^2-(n3/n1)^2)/((1-(n3/n1)^2)*((1+(n3/n1)^2)*(sin(theta)^2)-
(n3/n1)^2))):
> Eyo:=4*(cos(theta))^2/(1-(n3/n1)^2):
> Ezo:=(4*(cos(theta))^2*((sin(theta))^2)/((1-(n3/n1)^2)*((1+(n3/n1)^2)*(sin(theta)^2)-(n3/n1)^2))):
> evalf(Exo); evalf(Eyo); evalf(Ezo);
```

```
1.650932897

2.038925901

2.325328201
```

Calculation of Gibbs Surface Excess (Hansen method)

Penetration Depth value

```
> d:=lamda/(4*Pi*Im(xi3)):
> evalf(d);
```

$.1683838193\,10^{-6}\ meter$

Evaluation of beff for unpolarized experiment "unp", isotropic absorber "iso"

Polarization Ratio: see D:\Data-FTIR\MathCad\Gibbs Surface Excess.mcd

```
> PR:=0.5633:
> beff_s:=(d*Ey*n3)/(n1*cos(theta)):
> beff_p:=(d*Ex*n3)/(n1*cos(theta))+(d*Ez*n3)/(n1*cos(theta)):
> beff_unp:=((PR*beff_s)/(PR+1))+(beff_p/(PR+1)):
> evalf(beff_unp);
```

$.3435962706\,10^{-6}\ meter$

Input Integrated Absorbance Data

```
> Abs:=0.522428:
```

Calculation of Gibbs Surface Excess from Integrated Absorbance

```
> Cit:=(Abs-(N*epsilon*Conc*beff_unp))/(N*epsilon*(beff_unp/d)):
> evalf(Cit);
```

$.6052028312\,10^{-5}\ \frac{mol}{meter^2}$

```
> evalf(Cit)*((1*meter^2)/(10^18*nm^2))*((6.0221367e23*molecule)/mol);
```

$3.644614181\ \frac{molecule}{nm^2}$

A.4 GIBBS SURFACE EXCESS FROM INTEGRATED -LOG(R) AT 2910 RECIPROCAL CENTIMETERS

Gibbs Surface Excess from Integrated -log(R) ATR Spectra

Based on Mean Square Electric Fields Calculated from Derivations by Wilford Hansen
with Sperline Polarization Ratio Modification

Filename: Gibbs Surface Excess @ 2910.mws (60 degree incident angle)
Date: 30 October 2002

References:

1. Hansen, W. N. *Jnl of the Optical Society of America* 1968, *58*, 380
2. Hansen, W. N. Internal reflection spectroscopy in electrochemistry. *Advances in Electrochemistry and Electrochemical Engineering* 1973, *9*, 1-60
3. Hansen, W. N. *Analytical Chemistry* 1966, *38*, 1810
4. Citra, M. J.; Axelsen, P. H. *Biophysical Journal* 1996, *71*, 1796
5. Picard, F.; Buffeteau, T.; Desbat, B.; Auger, M. Pezolet, M. *Biophysical Journal* 1999, *76*, 539
6. D:\MathCad\Gibbs Surface Excess.mcd

Experimental Parameter Inputs

> restart:

Number of internal reflections

> N:=22:

Concentration of Bulk Solution

> Conc:=0.004001*mol/(1E-1*meter)^3;

$$Conc := 4.001000000 \frac{mol}{meter^3}$$

Transmission molar extinction coefficient

> epsilon:=3616785.0*(1/meter)*((1E-1*meter)^3/mol);

$$\varepsilon := 3616.7850 \frac{meter^2}{mol}$$

Incident angle

> theta:=(49.332/180)*Pi:

Wavelength

> lamda:=(291000*meter^(-1))^(-1):

> evalf(lamda);

$$.3436426117\,10^{-5}\ meter$$

Medium 1 complex refractive index input

```
> n1:=3.4302:
> k1:=0.0000:
> n1_cpx:=Complex(n1,k1);
```

$$n1\_cpx := 3.4302 + 0.\,I$$

Medium 2 complex refractive index input

```
> n2:=1.236:
> k2:=0.00222:
> n2_cpx:=Complex(n2,k2);
```

$$n2\_cpx := 1.236 + .00222\,I$$

Second medium thickness

```
> h:=(0E-9)*meter;
```

$$h := 0.$$

Mean square electric field strength calculated at distance z from the n1|n2 interface

```
> z:=(0E-9)*meter;
```

$$z := 0.$$

Medium 3 complex refractive index input

```
> n3:=1.236:
> k3:=0.00222:
> n3_cpx:=Complex(n3,k3);
```

$$n3\_cpx := 1.236 + .00222\,I$$

Calculation of Mean Square Electric Fields

Define xi for n1, n1|n2, and n2|n3 interface

```
> xi1:=n1_cpx*cos(theta):
> xi2:=sqrt((n2_cpx^2)-(n1^2)*(sin(theta))^2):
> xi3:=sqrt((n3_cpx^2)-(n1^2)*(sin(theta))^2):
```

Beta for second medium

```
> beta:=2*Pi*xi3*(h/lamda):
```

Fresnel Coefficients for the n1|n2 interface

```
> rs12:=(xi1-xi2)/(xi1+xi2):
> rp12:=(n2_cpx^2*xi1-n1_cpx^2*xi2)/(n2_cpx^2*xi1+n1_cpx^2*xi2):
> ts12:=2*xi1/(xi1+xi2):
> tp12:= 2*n2_cpx^2*xi1/(n2_cpx^2*xi1+n1_cpx^2*xi2):
```

Fresnel Coefficients for the n2|n3 interface

```
> rs23:=(xi2-xi3)/(xi2+xi3):
> rp23:=(n3_cpx^2*xi2-n2_cpx^2*xi3)/(n3_cpx^2*xi2+n2_cpx^2*xi3):
> ts23:=2*xi2/(xi2+xi3):
> tp23:= 2*n3_cpx^2*xi2/(n3_cpx^2*xi2+n2_cpx^2*xi3):
```

Combined Fresnel Coefficients for s and p components

```
> ts := ts12*ts23*exp(I*beta)/(1+rs12*rs23*exp(2*I*beta)):
> tp := (n1/n3_cpx)*(tp12*tp23*exp(I*beta))/(1+rp12*rp23*exp(2*I*beta)):
```

Exact mean square electric field strengths in the x, y, and z directions

```
> Ex:=((abs(tp*xi3/n3_cpx))^2)*exp(-4*Pi*(z-h)*Im(xi3)/lamda):
> Ey:=((abs(ts))^2)*exp(-4*Pi*(z-h)*Im(xi3)/lamda):
> Ez:=((abs(tp*n1*sin(theta)/n3_cpx))^2)*exp(-4*Pi*(z-h)*Im(xi3)/lamda):
> evalf(Ex); evalf(Ey); evalf(Ez);
```

1.670137892

1.951163784

2.156899605

Approximate mean square electric field strengths (Harrick approximation)

```
> Exo:=(4*(cos(theta))^2*((sin(theta))^2-(n3/n1)^2)/((1-(n3/n1)^2)*((1+(n3/n1)^2)*(sin(theta)^2)-(n3/n1)^2))):
> Eyo:=4*(cos(theta))^2/(1-(n3/n1)^2):
> Ezo:=(4*(cos(theta))^2*((sin(theta))^2)/((1-(n3/n1)^2)*((1+(n3/n1)^2)*(sin(theta)^2)-(n3/n1)^2))):
> evalf(Exo); evalf(Eyo); evalf(Ezo);
```

1.671853228

1.952186376

2.159118089

Calculation of Gibbs Surface Excess (Hansen method)

Penetration Depth value

```
> d:=lamda/(4*Pi*Im(xi3)):
> evalf(d);
```

$.1194433251\,10^{-6}\ meter$

Evaluation of beff for unpolarized experiment "unp", isotropic absorber "iso"

Polarization Ratio: see D:\Data-FTIR\MathCad\Gibbs Surface Excess.mcd

```
> PR:=0.5655:
> beff_s:=(d*Ey*n3)/(n1*cos(theta)):
> beff_p:=(d*Ex*n3)/(n1*cos(theta))+(d*Ez*n3)/(n1*cos(theta)):
> beff_unp:=((PR*beff_s)/(PR+1))+(beff_p/(PR+1)):
> evalf(beff_unp);
```

$.2079988009\,10^{-6}\ meter$

Input Integrated Absorbance Data

```
> Abs:=0.522428:
```

Calculation of Gibbs Surface Excess from Integrated Absorbance

```
> Cit:=(Abs-(N*epsilon*Conc*beff_unp))/(N*epsilon*(beff_unp/d)):
> evalf(Cit);
```

$.3292461228\,10^{-5}\ \frac{mol}{meter^2}$

```
> evalf(Cit)*((1*meter^2)/(10^18*nm^2))*((6.0221367e23*molecule)/mol);
```

$1.982765159\ \frac{molecule}{nm^2}$